Bioactive Materials 43 (2025) 129–144

Contents lists available at ScienceDirect

Bioactive Materials

journal homepage: www.keaipublishing.com/en/journals/bioactive-materials

A polymer nanogel-based therapeutic nanovaccine for prophylaxis and direct treatment of tumors *via* a full-cycle immunomodulation

Yunqi Guo [a], Zhiqiang Wang [a], Gaoming Li [a], Mengsi Zhan [a], Tingting Xiao [b], Jianhong Wang [c], Jan C.M. van Hest [c,**], Xiangyang Shi [a,*], Mingwu Shen [a,***]

[a] *State Key Laboratory for Modification of Chemical Fibers and Polymer Materials, Shanghai Engineering Research Center of Nano-Biomaterials and Regenerative Medicine, College of Biological Science and Medical Engineering, Donghua University, Shanghai, 201620, PR China*
[b] *Institute of Frontier Medical Technology, College of Chemistry and Chemical Engineering, Shanghai University of Engineering Science, Shanghai, 201620, PR China*
[c] *Bio-Organic Chemistry, Department of Biomedical Engineering, Institute for Complex Molecular Systems (ICMS), Eindhoven University of Technology, Eindhoven, 5600, MB, the Netherlands*

ARTICLE INFO

Keywords:
PVCL nanogels
Apoptotic cancer cell membranes
Therapeutic nanovaccine
STING activation
Direct therapy-assisted full-cycle immunomodulation

ABSTRACT

Construction of a cancer nanovaccine that can simultaneously activate immune cells and exert efficient tumor treatment still remains a challenge. Herein, we showcase a proof-of-concept demonstration of an advanced therapeutic nanovaccine formulation based on poly(*N*-vinylcaprolactam) nanogels (NGs) which were loaded with manganese dioxide (MnO_2), the sonosensitizer chlorin e6 (Ce6), and the immune adjuvant cyclic GMP-AMP (cGAMP). The gels were furthermore coated with apoptotic cancer cell membranes (AM). On the one hand, the AM promoted the recognition of NGs by antigen presenting cells (APCs) in lymph nodes due to their enhanced immunogenicity, then the loaded Mn and cGAMP could mature APCs *via* stimulator of interferon genes (STING) activation for triggering immunity to prevent tumor growth. On the other hand, the NGs could selectively release Mn^{2+} for hydroxyl radical production and Ce6 to generate single oxygen under ultrasound irradiation of tumors, respectively, thereby exerting local chemodynamic/sonodynamic therapy to induce immunogenic cell death (ICD). Moreover, the Mn^{2+} could also activate STING in tumors to synergize with ICD for potentiated immune responses. Overall, the biomimetic NG-based therapeutic nanovaccine could directly evoke immune system, and also conduct local tumor treatment to further activate ICD, thus realizing a full-cycle immunomodulation (tumor killing for ICD/antigen production, and tumor cells/APCs immune activation) to tackle bilateral tumor growth.

1. Introduction

Cancer nanovaccines that can train the immune system to be sensitive to tumor antigens have obtained great attention as an emerging immune therapeutic modality for tumor inhibition [1–4]. A typical cancer nanovaccine is always composed of tumor-associated antigens (TAAs) for specificity, adjuvants for immune activation, and nanocarriers for enhanced delivery [5–7]. Currently, most nanovaccines only carry model antigen, such as ovalbumin, to directly counter single antigen target [8–10]. However, such nanovaccines may not be able to elicit sufficient immune responses due to the continuous progress and genetic heterogeneity of tumors. Thus, a next generation of nanovaccine formulation requires to integrate abundant TAAs to achieve the threshold for triggering satisfactory antitumor immunity. Recently, biomimetic nanotechnology that can inherent proteins from living cells to endow the nanovaccines with unique features has provided a new direction for addressing the specific needs of immune activation [11].

Cancer cell membranes, easily extracted from cancer cells, have been widely used to camouflage nanodrugs for active tumor delivery, owing to the presence of homologous targeting proteins in the membrane [12]. Besides, cancer cell membranes bearing a complete membrane protein array have recently been proposed as ideal TAAs to construct nanovaccines, thereby triggering specific immune responses to the corresponding tumors [13,14]. However, the presence of immune

Peer review under responsibility of KeAi Communications Co., Ltd.
* Corresponding author.
** Corresponding author.
*** Corresponding author.
E-mail addresses: j.c.m.v.hest@tue.nl (J.C.M. van Hest), xshi@dhu.edu.cn (X. Shi), mwshen@dhu.edu.cn (M. Shen).

https://doi.org/10.1016/j.bioactmat.2024.09.024
Received 18 July 2024; Received in revised form 15 September 2024; Accepted 18 September 2024

escape-related proteins on cancer cell membranes may hinder the successful recognition of the nanovaccine by the immune system [15]. Although modifying targeting ligands on cancer cell membranes is promising to strengthen the vaccine delivery to immune cells, the synthesis process is generally complicated and the delivery efficacy is inefficient [6,16]. Encouraged by the design principle of *in situ* vaccines that utilize direct tumor treatment, such as chemotherapy, radiotherapy, or photothermal therapy to induce apoptosis and release TAAs for immunity stimulation [17,18], a rational choice to maximize the immunomodulatory capacity of cancer cell membranes is to induce the apoptosis of cancer cells before extraction. Due to the huge possibility of undergoing immunogenic cell death (ICD) in apoptotic cancer cells, the apoptotic cancer cell membranes (AM) are expected to also carry calreticulin (CRT), which is an essential ICD marker and mediates enhanced immune cell uptake for better immune activation [19–21].

Except for the TAAs, the antitumor effects of nanovaccines are also hampered by the immunosuppressive tumor microenvironment (TME) and insufficient tumor inhibition efficacy [22]. Thus, multifunctional nanovaccines enabling both immune activation and direct tumor killing may achieve enhanced tumor suppression performance. Nevertheless, this concept is greatly challenged by inducing undesirable side effects on immune cells when employing traditional cytotoxic antitumor drugs. Local treatment modalities that utilize different external energies or special signals to trigger therapy only at tumor sites have aroused increasing attention due to their non-invasiveness, specificity, and high efficiency [23,24]. As an emerging new modality, sonodynamic therapy (SDT) can generate cytotoxic single oxygen ($^1O_2$) *via* the synergy between sonosensitizer and ultrasound (US) to achieve tumor inhibition [25]. Compared with other modalities, SDT has the benefit of enhanced penetration of US in tumor tissue for improved tumor therapy [26,27].

Accumulating evidence has demonstrated that SDT is capable of inducing ICD to activate systemic antitumor immunity [28], laying the foundation for using SDT to strengthen the immunomodulation. Moreover, the produced reactive oxygen species (ROS) $^1O_2$ during SDT can cause irreparable deoxyribonucleic acid (DNA) damage and the damaged DNA can escape from the cell nucleus to cytosol [29–31]. Then the double-stranded DNA (dsDNA) located in the cytosol can be recognized and transformed by the cyclic guanosine monophosphate (GMP)-adenosine monophosphate (AMP) synthase (cGAS) to form 2′, 3′-cyclic GMP-AMP (cGAMP) for activating the stimulator of interferon genes (STING) pathway [32,33]. The activated cGAS-STING pathway promotes the secretion of type I interferon (IFN) and proinflammatory cytokines, which mature dendritic cells (DCs) and further activate T cells to induce adaptive immunity [34,35]. In addition to ROS and conventional STING activator, recent studies have indicated the potential of Mn^{2+} to directly stimulate cGAS, provoke the sensitiveness of cGAS to cytosolic dsDNA, as well as improve the binding efficacy of cGAMP to STING [36–40].

To maximize the advantages of cancer cell membranes, SDT, and Mn^{2+} in tumor treatment, it is important to choose a nanoplatform to integrate all the components. Poly(N-vinylcaprolactam) (PVCL) nanogels (NGs) are known as a widely investigated nanocarrier with good

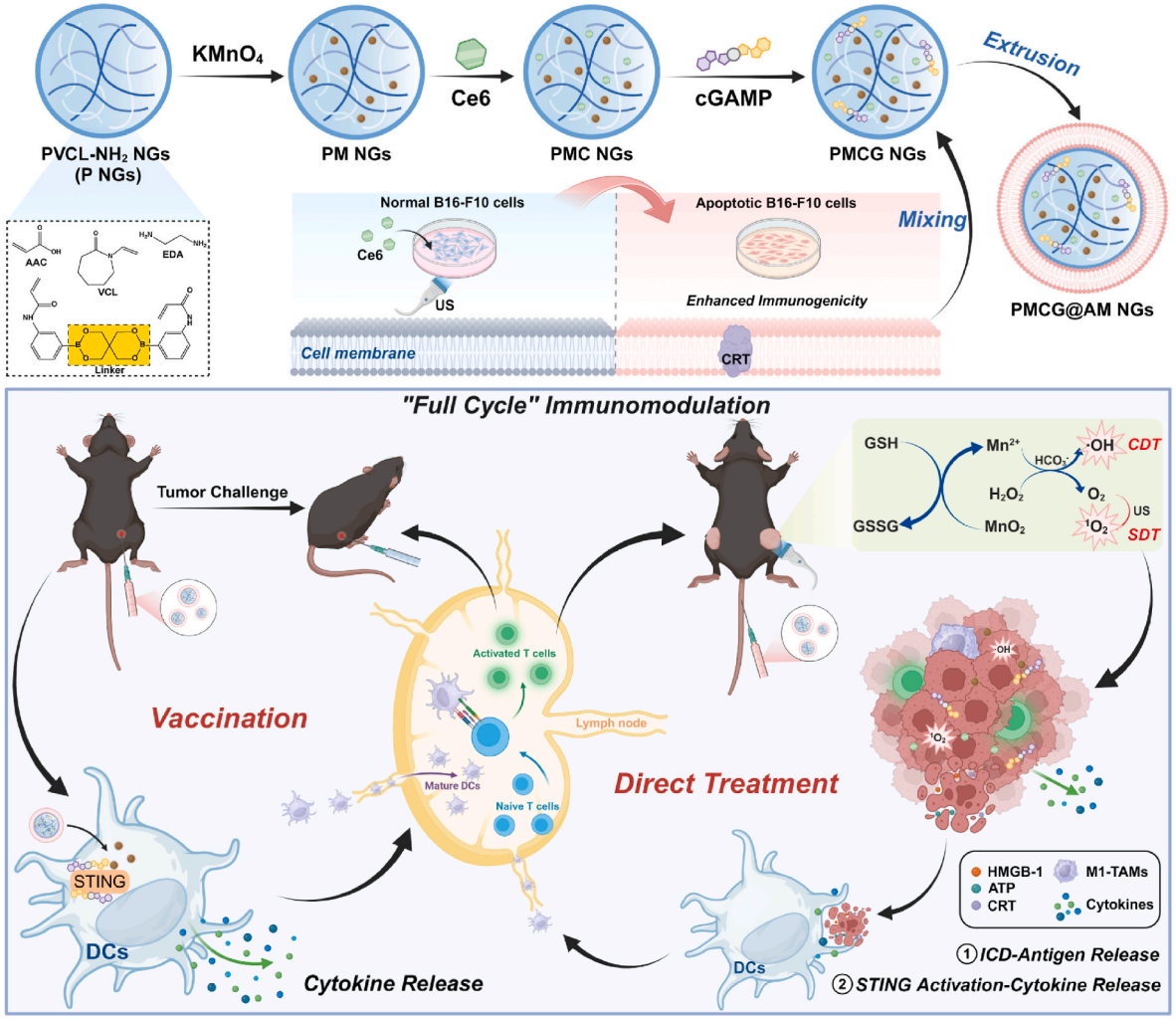

Scheme 1. Synthesis of PMCG@AM NGs for tumor prophylaxis and direct tumor treatment *via* a full-cycle immunomodulation.

biocompatibility, designable responsiveness, ideal drug loading capacity, as well as facile functionalization, thus realizing tumoral drug delivery with controlled release [41–43]. Most remarkably, the PVCL NGs prepared *via* a precipitation polymerization method can act as a nanoreactor for *in situ* synthesis of manganese dioxide nanoparticles (MnO_2 NPs) [44], which can be converted to Mn^{2+} for immune activation and chemodynamic therapy (CDT) *via* a Fenton-like reaction [45–47]. These unique merits highlight the feasibility to incorporate PVCL NGs with different therapeutic agents to construct a multifunctional nanovaccine.

In this work, we have developed a multifunctional nanovaccine composed of AM-camouflaged PCVL NGs loaded with MnO_2 NPs, sonosensitizer chlorin e6 (Ce6), and immune adjuvant cGAMP (Scheme 1). The PVCL NGs with pH/ROS-responsiveness were synthesized using a crosslinker containing boronic ester bonds *via* a precipitation polymerization method, after which MnO_2 NPs were loaded *in situ*. Next, Ce6 was encapsulated through Mn-N coordination bonding and cGAMP was loaded through electrostatic compression, followed by coating with AM. The developed NGs were thoroughly characterized, then used for *in vivo* vaccination or treatment of a bilateral tumor model utilizing the combined action of the loaded components. The obtained biomimetic NGs were expected to realize efficient tumor prophylaxis along with direct tumor treatment *via* a full-cycle immunomodulation, since they possessed significant features such as: (1) dual responsiveness of NGs that enabled selective NG dissociation in the TME for controlled drug release; (2) homologous tumor targeting specificity with amplified membrane protein immunogenicity using the extracted AM; (3) the joint effects of Mn^{2+}, cGAMP, and AM which allowed for maturation of DCs *via* STING activation as well as TAAs presentation to T cells for specific tumor prevention; and (4) the addition of US irradiation can trigger local SDT at tumor site along with the Mn^{2+}-mediated CDT to facilitate ICD of tumor cells, thus cooperating with NG-induced immunity to render the full-cycle immunomodulation for effective bilateral tumor suppression.

2. Materials and method

2.1. Synthesis of PVCL-MnO_2 (PM) NGs

PVCL-NH_2 NGs (P NGs) were first synthesized using a crosslinker containing boronic ester bonds through a precipitation polymerization method according to the literature [42,43]. Then, MnO_2 NPs were *in situ* synthesized within P NGs by a redox reaction between the primary amine groups and $KMnO_4$ according to the literature protocols [44].

2.2. Synthesis of PMCG NGs

For Ce6 loading, Ce6 (5 mg) was dissolved in 0.5 mL of DMSO and dropped into 5 mL PM NG solution (1 mg/mL), followed by stirring for 24 h at room temperature. The mixture was centrifuged at 12000 rpm for 8 min to remove the supernatant, then the precipitate was redispersed in water and re-centrifuged at 1000 rpm for 3 min. For cGAMP loading, cGAMP (1 mg) was dissolved in 1 mL of water and dropped into 1 mL PM-Ce6 NG (PMC NG) solution (2 mg/mL), followed by stirring for 24 h at room temperature. After that, the mixture solution was centrifuged at 12000 rpm for 8 min to remove the unloaded cGAMP in the supernatant and obtain the PMC-cGAMP NGs (for short, PMCG NGs) in the precipitate.

2.3. Extraction of AM and preparation of PMCG@AM NGs

For extracting AM, B16-F10 cells were incubated in T75 culture flasks, and treated with free Ce6 ([Ce6] = 5 μg/mL) for 6 h. Then, the cells were irradiated by US (1.0 MHz, 1.0 W/cm^2) for 2 min and incubated for additional 6 h. Next, the apoptotic cells were collected and the membranes (AM) were extracted by a membrane and cytosol protein extraction kit according to the manufacturer's instructions. For comparison, the normal cancer cell membranes (NM) were also extracted from untreated B16-F10 cells. For the synthesis of PMCG@AM NGs, the prepared PMCG NGs (200 μg) were mixed with 0.5 mL of AM suspension (harvested from 5×10^6 cells) and the mixture was extruded 11 times using an Avanti mini extruder (Avanti Polar Lipids, Inc., Alabaster, AL). Subsequently, the mixture was centrifuged at 12000 rpm for 8 min at 4 °C to obtain the PMCG@AM NGs in the precipitate. The PMCG@NM NGs were prepared under the same experimental conditions using NM suspension.

2.4. Cell culture and in vitro assays

DCs, RAW 264.7 cells (a mouse macrophage cell line), and B16-F10 cells (a murine melanoma cell line) were regularly cultured, passaged, and adopted for *in vitro* assays including cellular uptake assay, cytotoxicity assay, STING activation, DC maturation, macrophage repolarization, intracellular glutathione (GSH) and ROS measurements, cell apoptosis, as well as ICD detection.

2.5. Animal experiments

All animal experiments were carried out following the protocols approved by the Animal Care and Use Committee of Donghua University (Approval No. DHUEC-NSFC-2023-02) and also in accordance with the guidelines and regulations of National Ministry of Health of China. Healthy C57BL/6 mice were applied for *in vivo* vaccination and tumor challenge assay. A bilateral subcutaneous B16-F10 mouse tumor model was established for *in vivo* combined therapy and immune modulation evaluations. H&E staining of major organs as well as hematology and serum biochemistry analysis were performed to confirm the biosafety of the PMCG@AM NGs.

2.6. Statistical analysis

All experimental data were represented as the mean ± standard deviation through at least three experiments. One-way analysis of variance statistical method was used to analyze the experimental results through GraphPad Prism 8.0.2 software (San Diego, CA). A p value of 0.05 was selected as a significance level, and the data were indicated with (*) for $p < 0.05$, (**) for $p < 0.01$, and (***) for $p < 0.001$, respectively. Full experimental details can be seen in the Supporting Information.

3. Results and discussion

3.1. Synthesis and characterization of PMCG NGs

The synthesis route of PMCG NGs is shown in Scheme 1. First, P NGs containing boronic ester bonds were synthesized through a precipitation polymerization method and MnO_2 NPs were *in situ* formed within the P NGs through amine-mediated reduction of $KMnO_4$ to obtain PM NGs according to the literature [42,43]. The content of Mn in PM NGs was measured to be 4.9 % through inductively coupled plasma-optical emission spectroscopy. Then, Ce6 was loaded within the PM NGs *via* Mn-N coordinate bonding to prepare PMC NGs. The feed mass ratio of PM NGs/Ce6 was optimized (Table S1), and a mass ratio of 1: 1 was selected to achieve a balanced encapsulation efficiency (EE, 69.3 %) and loading content (LC, 40.9 %). Finally, cGAMP was physically loaded within the PMC NGs through electrostatic interaction to yield PMCG NGs. As shown in Table S2, at the optimal PMC NGs/cGAMP mass ratio of 1: 0.5, the EE and LC of cGAMP were measured to be 58.3 % and 22.6 %, respectively through UV–vis spectrometry.

Subsequently, the hydrodynamic sizes and zeta potentials of the as-prepared NGs were tested (Table S3). The synthesized PMCG NGs exhibited an increased hydrodynamic size of 164.5 ± 2.1 nm and a decreased zeta potential of −6.4 ± 1.3 mV compared with P NGs (125.4 ± 5.8 nm, 12.3 ± 2.1 mV), PM NGs (143.1 ± 3.2 nm, 5.4 ± 0.5 mV) and

PMC NGs (152.3 ± 2.2 nm, 3.8 ± 0.3 mV) due to the loading of MnO_2 NPs, Ce6, and cGAMP. Scanning electron microscopy (SEM) was next performed to observe the morphology of the different NGs. Clearly, P, PM, and PMCG NGs all possessed a uniform spherical morphology and PMCG NGs displayed the largest average size (86.1 ± 3.3 nm) among the three NG formulations, reconfirming the formation of NGs and the loading of multiple components (Figure S1 and Fig. 1A). It is worth noting that the hydrodynamic size of PMCG NGs is larger than that measured by SEM, likely due to the fact that the hydrodynamic size measured by dynamic light scattering reflects the size of NGs in an expanded state when dispersed in water, while the SEM just determines the size of the shrunken NGs in a dry state.

Fluorescence emission spectra and UV–vis spectra were then applied to verify the loading of Ce6. As shown in Fig. S2, PMCG NGs displayed a similar maximum emission wavelength to that of free Ce6 at an excitation wavelength of 400 nm, which not only demonstrates the loading of Ce6, but also indicates the capacity of PMCG NGs for fluorescence imaging. Besides, PMCG NGs showed the characteristic UV–vis absorption peaks of both Ce6 (400 nm and 660 nm) and cGAMP (260 nm), suggesting the successful co-encapsulation of Ce6 and cGAMP within the NGs (Fig. 1B).

Then, the stimuli-responsiveness of PMCG NGs was analyzed through recording the changes of their hydrodynamic size distribution under different conditions. As displayed in Fig. S3, the one sharp peak of

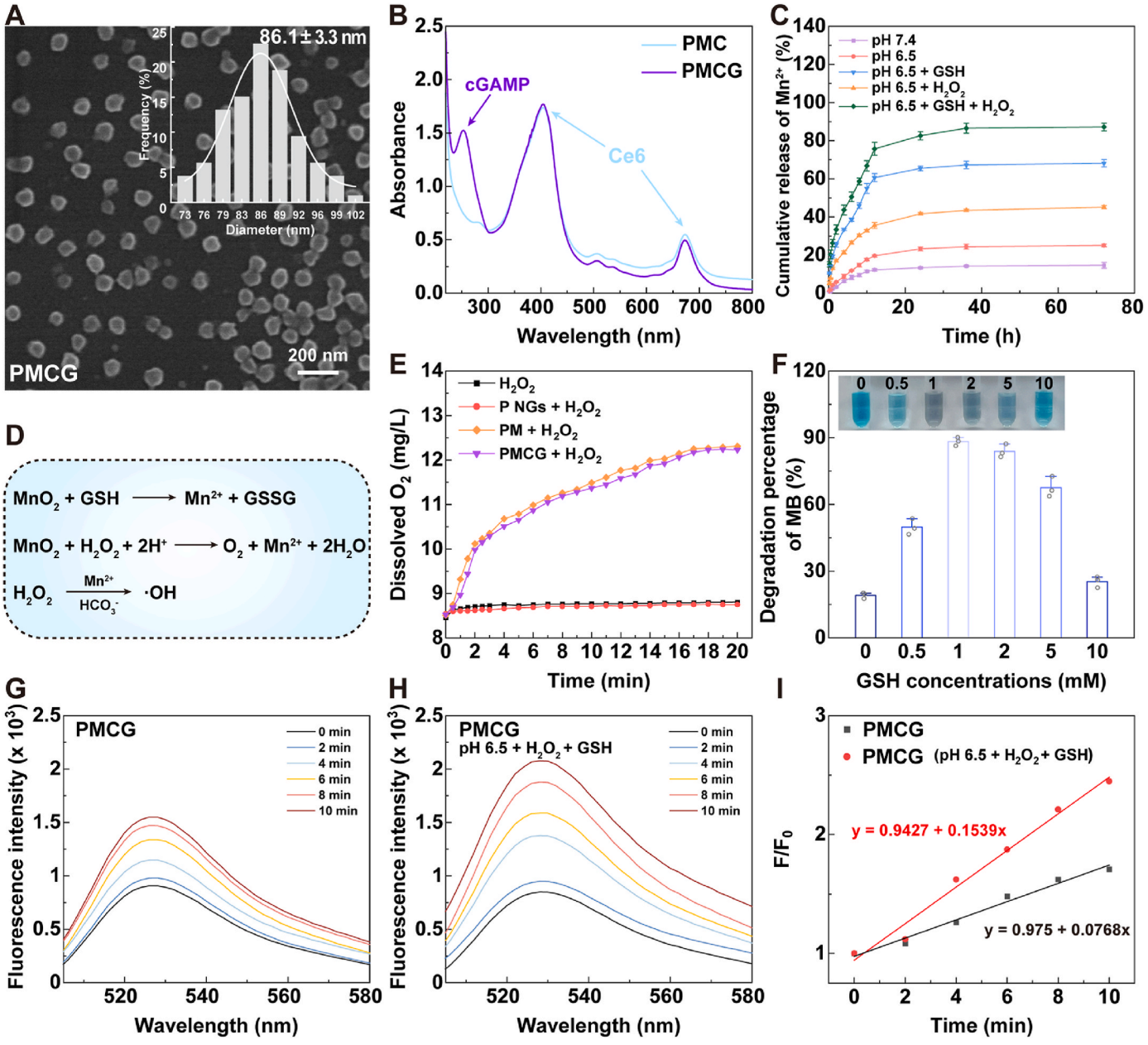

Fig. 1. (A) SEM image of PMCG NGs. (B) UV–vis spectra of PMC and PMCG NGs. (C) Cumulative release of Mn^{2+} from PMCG NGs exposed to different buffer solutions ([GSH] = 1 mM and [H_2O_2] = 100 μM, n = 3). (D) Equations related to the transformation of MnO_2 under different conditions. (E) Generation of O_2 in H_2O_2 solution or H_2O_2 solution containing P, PM, or PMCG NGs as a function of incubation time ([H_2O_2] = 100 μM). (F) Methylene blue (MB) degradation percentage and corresponding photograph (inset) of MB solution after treated with PMCG NGs at different GSH concentrations. Time-dependent $^1O_2$ generation in (G) PMCG NG dispersion in PBS or (H) PMCG NG dispersion containing H^+ (pH 6.5 phosphate buffer), 100 μM H_2O_2 and 1 mM GSH after US irradiation (1.0 MHz, 1.0 W/cm^2), as well as (I) the corresponding rate constant of $^1O_2$ generation (F_0 and F represent the fluorescence intensity of O21 probe at 530 nm before and after US irradiation for different time periods, respectively).

PMCG NG dispersion changed to a broad peak after incubating with phosphate buffer (pH 6.5), and the further addition of H_2O_2 (100 μM) led to a more noticeable change in the size distribution, namely the appearance of multiple peaks. These results suggest the disintegration of PMCG NGs under an acidic and H_2O_2-rich condition *via* boronic ester bond cleavage, indicating the pH- and ROS- responsiveness of PMCG NGs. Considering that the MnO_2 NPs can be easily transformed to Mn^{2+} under GSH-rich or acidic/H_2O_2-rich conditions (Fig. 1D), we then checked the selective release of Mn^{2+} from PMCG NGs under different conditions. Under a normal physiological condition (pH 7.4), only 14.7 % of Mn^{2+} was released from the NGs within the monitoring time period of 72 h (Fig. 1C). The release of Mn^{2+} increased to 25.1 % at an acidic pH of 6.5, which is presumably due to the decomposition of a small portion of MnO_2 NPs by H^+ to form Mn^{2+}. In the presence of H^+ and H_2O_2 or GSH, the release of Mn^{2+} reached a level of 45.1 % (pH 6.5 + H_2O_2) and 68.2 % (pH 6.5 + GSH) within 72 h, respectively. Furthermore, 87.2 % of Mn^{2+} release was achieved under the condition of pH 6.5 + GSH + H_2O_2, indicating that the loaded MnO_2 NPs can be largely reduced to Mn^{2+} in response to the TME. In general, the above results suggest that the PMCG NGs are relatively stable at a physiological condition to prevent Mn^{2+} leakage, but selectively dissociate and release the bioactive Mn^{2+} in a simulated TME, laying the foundation for Mn^{2+}-mediated CDT of tumors and antitumor immune activation.

As O_2 should be generated during the decomposition of MnO_2 NPs in the acidic/H_2O_2-rich environment, we therefore analyzed the generation of O_2 in 100 μM H_2O_2 solution (pH 6.5) containing P, PM or PMCG NGs by a multiparameter benchtop meter. Contrary to the P NG dispersion that did not display obvious O_2 generation (similar to the NG-free H_2O_2 solution), both PM and PMCG NGs containing MnO_2 NPs enabled rapid production of O_2, demonstrating the ability of loaded MnO_2 NPs to produce O_2 during the process of Mn^{2+} generation *via* decomposition of H_2O_2 (Fig. 1E). It is worth mentioning that the enhanced O_2 level has a beneficial effect on tumor treatment through both hypoxia relief and SDT promotion.

Considering that Mn^{2+} can decompose H_2O_2 to yield toxic ·OH through a Fenton-like reaction, we next evaluated the ability of free Mn^{2+} or PMCG NGs to produce ·OH *via* monitoring the degradation of methylene blue (MB) [41]. As shown in Fig. S4, free Mn^{2+} significantly decreased the absorbance of MB at 665 nm in the presence of H_2O_2 and HCO_3^-, which means that Mn^{2+} can react with H_2O_2 to generate ·OH within the physiological microenvironment, in agreement with the literature [41]. Since the PMCG NGs were able to produce Mn^{2+} in the presence of GSH, the Mn^{2+}-mediated Fenton-like reactivity of PMCG NGs under different GSH concentrations was then verified (Fig. 1F). The degradation percentage of MB first increased with the increase of GSH concentration from 0.5 to 1 mM, while the MB degradation decreased in excess of GSH (2−10 mM). The inset in Fig. 1F showed that the solution blue color faded at low GSH concentrations and gradually remained blue with the increase of GSH concentration, in consistency with the quantitative results. The obstructed MB degradation at relatively high GSH concentrations is likely due to the elimination of generated ·OH by GSH. In any case, benefiting from the conversion of MnO_2 NPs to Mn^{2+} that consumes a certain amount of GSH, the PMCG NGs should enable more efficient CDT than free Mn^{2+} since free Mn^{2+} has no ability to deplete GSH that can capture ·OH.

Having confirmed the ability of PMCG NGs to generate ·OH, we next analyzed the SDT potential of PMCG NGs by detecting the $^1O_2$ generation efficiency under US irradiation. The fluorescence intensity of the BBoxiProbe® O21 probe was measured to test the generation of $^1O_2$, which can oxidize the probe, leading to the display of green fluorescence. Due to the existence of the sonosensitizer Ce6, the fluorescence intensity of O21 in PMCG NG dispersion gradually increased with the increase of US irradiation time (Fig. 1G). Interestingly, as depicted in Fig. 1H, the PMCG NG dispersion containing H^+, H_2O_2 and GSH was able to increase the fluorescence intensity of O21 more quickly under US irradiation. Moreover, the oxidized O21 generation rate constant under this condition was measured to be 0.1539 min^{-1} (Fig. 1I), which is 2 times higher than that of the PMCG NG dispersion (0.0768 min^{-1}) in PBS. These results suggest that the efficiency of PMCG NGs to produce $^1O_2$ under US irradiation is significantly enhanced in a simulated TME, likely due to the improved release of Ce6 and generation of O_2.

3.2. Synthesis and characterization of PMCG@AM NGs

We utilized free Ce6 and US to induce the apoptosis of B16-F10 cells before AM extraction (Fig. 2A). First, to optimize the timing for US irradiation, the cellular uptake of free Ce6 in B16-F10 cells at different incubation time points was evaluated by flow cytometry. As shown in Fig. S5, at the same Ce6 concentration, the intracellular fluorescence intensity of Ce6 gradually increased when the incubation time increased from 1 h to 6 h, and the cellular uptake of Ce6 did not significantly increase when the incubation time was further elongated to 8 h. Therefore, we decided to perform the US irradiation on B16-F10 cells after the cells were treated with Ce6 for 6 h. Next, to confirm the Ce6-induced SDT under US irradiation, the intracellular ROS generation as the major indicator of SDT was evaluated (Fig. 2B and C). B16-F10 cells treated only with Ce6 showed no significant increase in fluorescence intensity associated with the ROS level, while the addition of US enabled greatly increased ROS generation, demonstrating the successful implementation of SDT. Lastly, the efficiency of Ce6 and US to induce cell apoptosis was analyzed by flow cytometry. The treatment of Ce6 alone did not obviously influence the cell apoptosis degree, while the further US irradiation increased the percentage of apoptotic cells in a Ce6 concentration-dependent manner, suggesting that the Ce6 under US irradiation can exert an SDT effect to induce cell apoptosis (Fig. S6A). Quantitative data revealed that the cell apoptosis rate was more significant when the concentration of Ce6 increased to 5 or 10 μg/mL with US irradiation, whereas the cell necrosis rate dramatically increased at a Ce6 concentration of 10 μg/mL (Fig. 2D and Figs. S6B–C). Therefore, to avoid excess necrosis and harvest cell membranes at an apoptotic state, 5 μg/mL of Ce6 under US irradiation was selected to treat B16-F10 cells before AM extraction.

To investigate the changes in cell membrane protein composition, the proteomics of B16-F10 cells before and after apoptosis was analyzed. As shown in Fig. S7A, 1520 upregulated proteins and 1752 down regulated proteins were confirmed in the Ce6 + US group relative to the negative control PBS group. Subsequently, the subcellular localization of these differential proteins (DEPs, totally 3272) was predicted, and the results showed that 13.08 % of DEPs was localized on the plasma membrane, meaning that the treatment of Ce6 under US irradiation can alter the protein composition of the cell membrane (Figs. S7B–C). Then, the DEPs located on the plasma membranes were classified according to the biological process of Gene Ontology (GO) analysis (Fig. 2E). It was found that totally 67 DEPs were related to the immune system process, suggesting that the Ce6/US-induced apoptosis may influence the expression of immune-related proteins on cell membranes, thereby regulating the immunoactivity of cell membranes. To confirm this hypothesis, the expression level of CRT on the cell membranes was further analyzed by Western blotting (WB), since CRT serves as a typical marker to reflect the immunogenicity degree. CRT level on the cell membranes was only found to be up-regulated when cells were treated with Ce6 in combination with US irradiation, demonstrating that the joint conduction of Ce6 and US can induce ICD to promote CRT exposure, and also suggesting that the cell membranes possess enhanced immunogenicity in this situation (Fig. S6D). In summary, the AM extracted from Ce6/US-treated B16-F10 cells are expected to better stimulate immune cells thanks to the increased presence of immunogenicity marker.

Afterwards, the extracted AM were coated onto PMCG NGs through a co-extrusion method to prepare PMCG@AM NGs. A TEM image showed that the size of PMCG@AM NG was around 115 nm and multiple membrane fragments were wrapped around the surface of the NG particle, validating the coating of AM (Fig. 2F and Fig. S8). Then, sodium

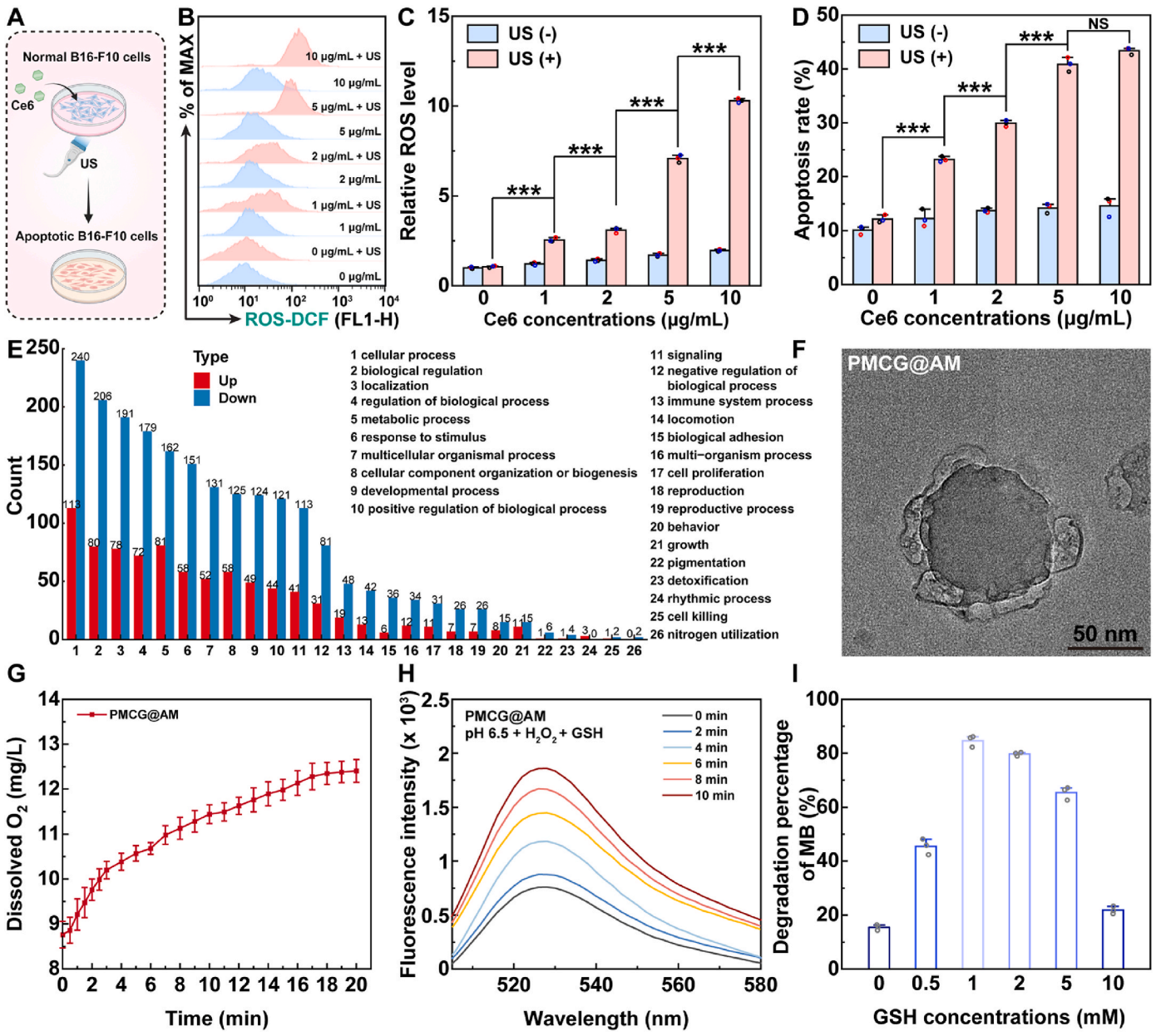

Fig. 2. (A) Schematic illustration of using Ce6 and US to induce apoptosis of B16-F10 cells. (B) Flow cytometry analysis and (C) quantification of intracellular ROS level in B16-F10 cells after different treatments for 6 h (n = 3). (D) Quantified apoptosis rate after different treatments (n = 3). (E) Up or down-regulated membrane proteins and their association with biological processes based on GO annotation. (F) TEM image of PMCG@AM NGs. (G) Generation of O_2 in 100 μM H_2O_2 solution containing PMCG@AM NGs as a function of incubation time (n = 3). (H) Time-dependent $^1O_2$ generation in PMCG@AM NG dispersion under a simulated TME condition (pH 6.5 + 100 μM H_2O_2 solution + 1 mM GSH) after US irradiation (1.0 MHz, 1.0 W/cm^2). (I) Degradation percentage of MB mixed with PMCG@AM NGs at different GSH concentrations (n = 3). For (B–D), the parameters of US were set as: 1.0 MHz, 1.0 W/cm^2, and 2 min. In parts C-D, * is for $p < 0.05$, ** is for $p < 0.01$, and *** is for $p < 0.001$, respectively.

dodecyl sulfate-polyacrylamide gel electrophoresis (SDS-PAGE) was conducted to verify the retention of membrane proteins on PMCG@AM NGs after co-extrusion. For comparison, NM were also extracted and tested. As illustrated in Fig. S9, AM and NM both showed protein bands, suggesting that the extracted cell membranes carried sufficient membrane proteins. As expected, the proteins of AM were retained on the NGs since the protein bands of AM and PMCG@AM NGs showed no significant difference. For subsequent experiments, NM-coated NGs (PMCG@NM NGs) were also prepared for comparison. The hydrodynamic size and zeta potential of PMCG@NM NGs were analyzed to confirm the coating of NM. As shown in Fig. S10A, similar to PMCG@AM NGs, the hydrodynamic size of PMCG@NM NGs increased and the zeta potential of PMCG@NM NGs decreased compared to the uncoated NGs, suggesting the successful decoration of NM.

In addition, PMCG@AM NGs displayed good colloidal stability in water, PBS, and completed Dulbecco's Modified Eagle Medium (DMEM) as their hydrodynamic sizes showed no significant change for at least 7 days (Fig. S10B). More importantly, the PMCG@AM NGs are still able to generate O_2 (Fig. 2G), produce $^1O_2$ under US irradiation (Fig. 2H), as well as yield ·OH to degrade MB (Fig. 2I), suggesting that the coating of AM does not seem to significantly influence the physicochemical properties of PMCG NGs.

3.3. *PMCG@AM NGs for in vitro immune activation*

Before analyzing the *in vitro* bioactivity of PMCG@AM NGs, their

cellular uptake behaviors in different cell lines were investigated first and compared with those of PMCG or PMCG@NM NGs. The Mn amounts taken up in B16-F10 cells treated with PMCG@NM or PMCG@AM NGs were significantly higher ($p < 0.001$) than those treated with PMCG NGs, illustrating that the cell membrane decoration can facilitate the cellular uptake *via* homologous targeting and cell adhesion molecule-promoted endocytosis (Fig. 3A). Moreover, the cellular uptake of different NG formulations in DCs or macrophages (RAW264.7 cells) was also analyzed to confirm the potential of NGs to be taken up by immune cells. As compared to PMCG NGs, PMCG@NM NGs displayed lower Mn uptake in both DCs and macrophages likely due to the fact that NM decoration renders NGs with immune escape effect. On the contrary, an obvious increase of Mn uptake was observed in DCs or macrophages after treatment with PMCG@AM NGs, possibly because the enhanced immunogenicity of AM makes the NGs easier to be recognized and phagocytosed by immune cells, which is conducive for antigen presentation and activation.

Afterwards, the cytotoxicity of PMCG@AM NGs in DCs or macrophages was analyzed *via* the cell counting kit-8 (CCK-8) assay to check their damage to immune cells. As depicted in Fig. 3B and C, PMCG NGs displayed no significant cytotoxicity to both DCs and macrophages because the Mn-mediated CDT and Ce6-mediated SDT were not triggered in immune cells. Although the treatment of PMCG@AM NGs slightly reduced their viabilities in a dose-dependent manner, the viabilities of both immune cells were maintained above 80 % at relatively low Ce6 concentrations (less than 10 μg/mL). In general, the efficient cellular uptake and mild cytotoxicity of PMCG@AM NGs in immune cells should facilitate the activation of specific immune responses.

Subsequently, to exploit the potential of PMCG@AM NGs as a nanovaccine, PMCG@AM NGs were directly incubated with immune cells, followed by analysis of cytokine release and cell phenotype (Fig. 3D). Considering that the PMCG@AM NGs mainly rely on the loaded adjuvant cGAMP to activate the cGAS-STING pathway in immune cells, the release of type I interferon (IFN-β) as well as another essential immune-related cytokine necrosis factor alpha (TNF-α) after different treatments was first detected. As shown in Fig. 3E–H, compared with the PBS or NM group, higher secretion levels of IFN-β and TNF-α were found in both DCs and macrophages (RAW264.7 cells) after AM treatment, suggesting that the AM can better stimulate the immune cells. Except for cGAMP, PM NGs that containing MnO_2 NPs also enabled the improved secretion of IFN-β and TNF-α, presumably due to the conversion of a portion of MnO_2 NPs to Mn^{2+} by H^+ in lysosomes after phagocytosis [48], and the generated Mn^{2+} has been proven to be a stimulator of cGAS-STING pathway [36]. As expected, the PMCG@AM NGs triggered the highest production of IFN-β and TNF-α among all groups ($p < 0.001$) due to the joint action of cGAMP, MnO_2 NPs, and AM, reflecting the most efficient STING stimulation and immune activation.

Encouraged by the improved cytokine release, the maturation of DCs after different treatments was next investigated *via* analysis of the expression of CD80 and CD86 (markers of matured DCs) through flow cytometry. In addition, according to the results of cytokine release experiments showing that P NGs did not significantly impact the expression levels of related cytokines and the PM NGs displayed effects similar

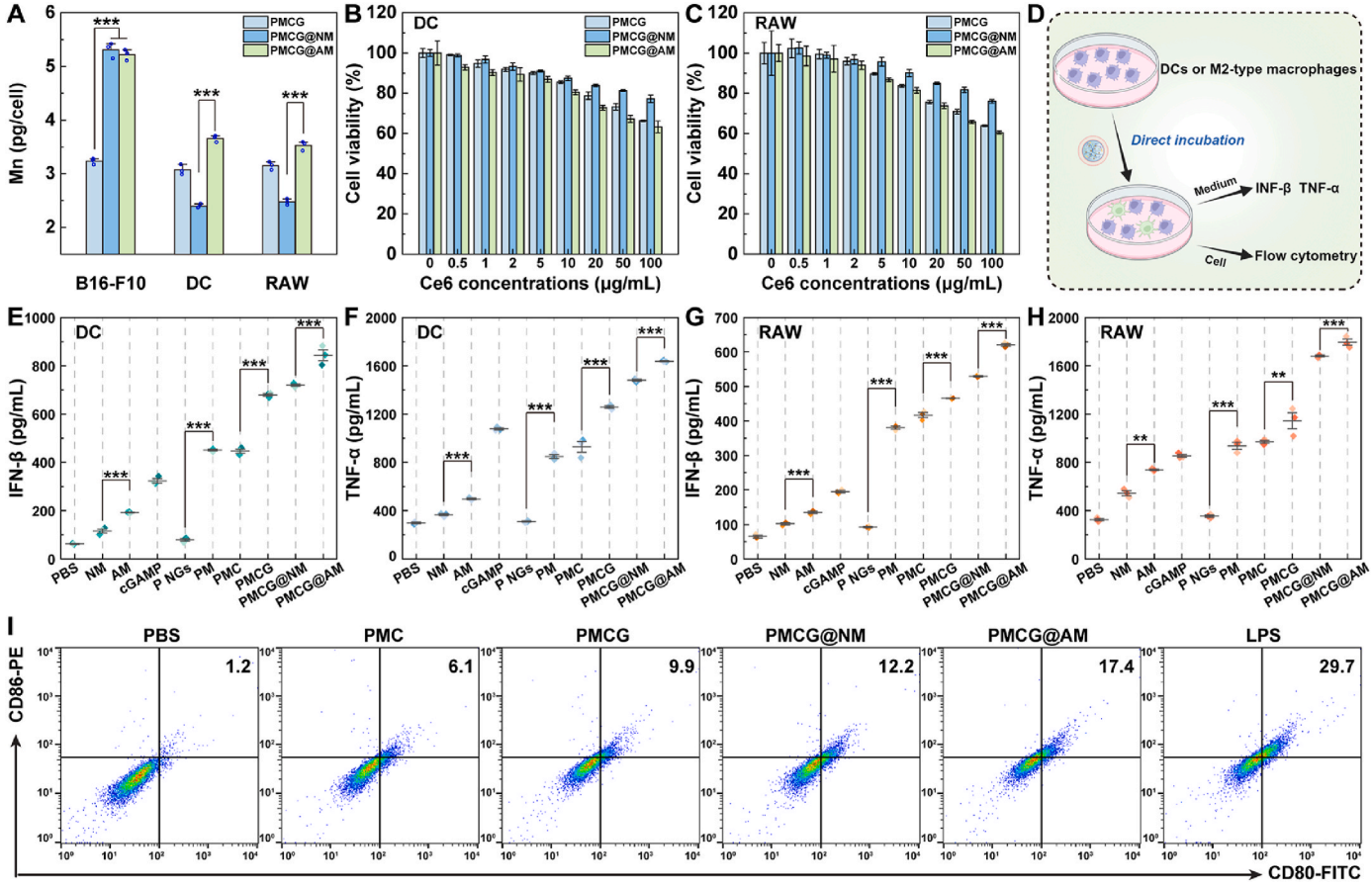

Fig. 3. (A) Mn uptake in B16-F10 cells, DCs, or RAW264.7 cells after treatment with PMCG, PMCG@NM, or PMCG@AM NGs at an Mn concentration of 1 μg/mL for 6 h (n = 3). Viabilities of (B) DCs and (C) RAW264.7 cells after treatment with PMCG, PMCG@NM, or PMCG@AM NGs at different Ce6 concentrations for 24 h (n = 6). (D) Schematic illustration of using PMCG@AM NGs to directly stimulate DCs or RAW 264.7 cells. Secretion of IFN-β and TNF-α in the culture medium of (E–F) DCs or (G–H) RAW264.7 cells after different treatments (n = 3). (I) Flow cytometry analysis of the DC maturation rate after direct incubation with different NGs for 24 h (n = 3, LPS-treated DCs were used as positive control). In parts A and E-H, * is for $p < 0.05$, ** is for $p < 0.01$, and *** is for $p < 0.001$, respectively.

to PMC NGs, we then just tested the PMC, PMCG, PMCG@NM, and PMCG@AM NGs in the flow cytometry experiments with PBS and LPS as negative and positive controls, respectively. As displayed in Fig. 3I and Fig. S11, the treatment of PMC NGs resulted in slight DC maturation (6.1 %) and the PMCG NGs containing cGAMP increased the maturity rate of DCs to 9.9 %, while the addition of NM coating led to 2.2 % matured DCs. It should be noted that although the uptake of PMCG@NM NGs in DCs is lower than that of PMCG NGs, the decoration of NM still contributes to the DC maturation, likely because the NM carry a significant amount of TAAs. The PMCG@AM NGs with enhanced cellular uptake led clearly to the highest level of DC maturation (17.4 %, $p < 0.001$), which was close to the positive control (lipopolysaccharide (LPS)-treated DCs).

Subsequently, the repolarization of macrophages was also tested *via* analysis of the expression of CD86 (a marker of M1-type macrophages) and CD206 (a marker of M2-type macrophages) through flow cytometry. Herein, in addition to the PBS group, normal macrophages were first stimulated by interleukin-4 (50 ng/mL) to prepare M2-type macrophages, then the M2-type macrophages were treated with different NGs or LPS. The treatment of PMCG@AM NGs led to the highest proportion of CD86 (7.8 %), the lowest proportion of CD206 (3.2 %), as well as the highest M1/M2 ratio among all groups except for the positive control (LPS-treated M2-type macrophages), which can be attributed to the effective STING activation and cytokine release (Fig. S12).

Lastly, to further verify the activation of STING in both DCs and macrophages after treated with the NGs, the expression levels of STING-

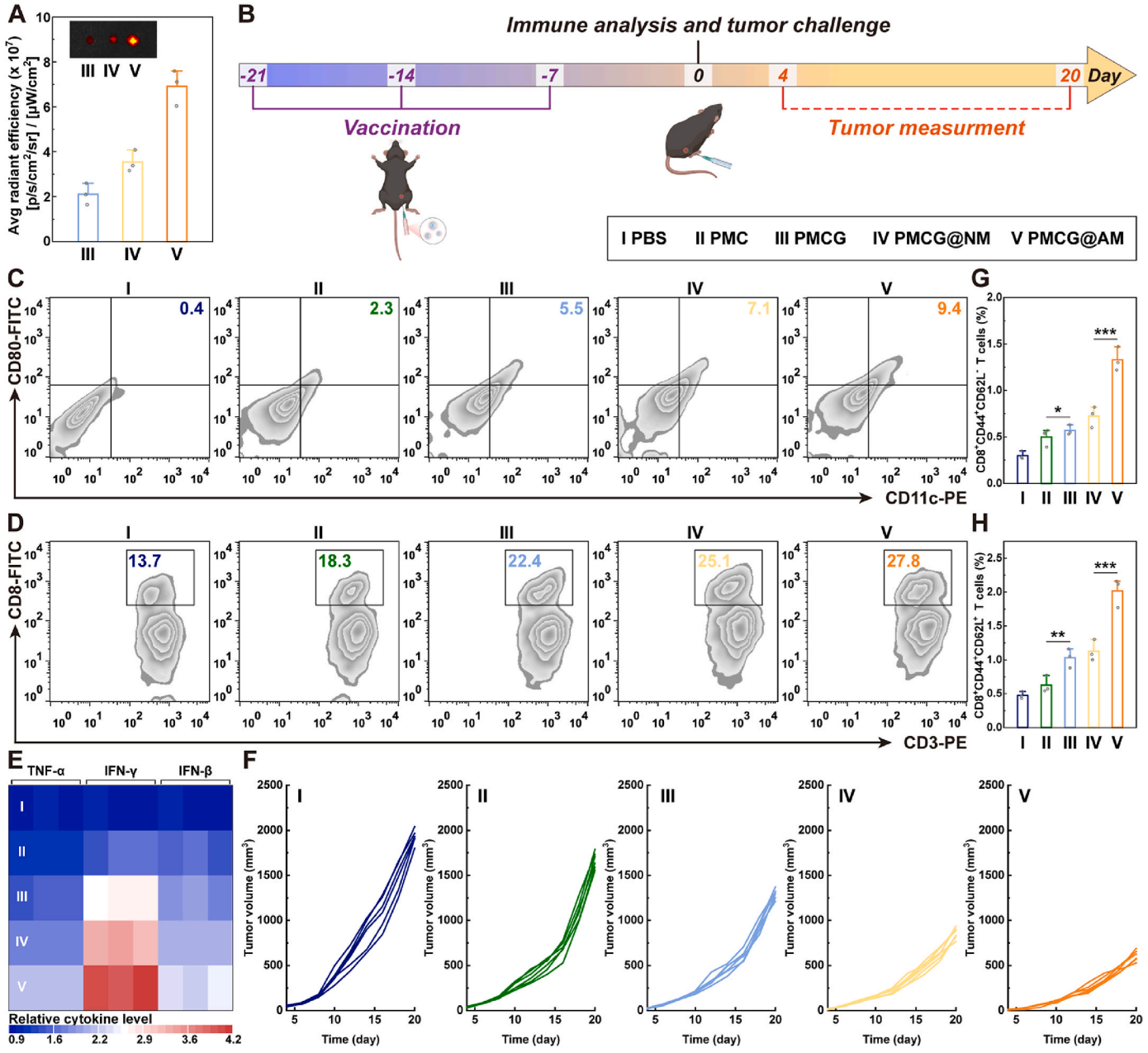

Fig. 4. (A) *Ex vivo* fluorescence image (inset) and quantitative fluorescence intensity of lymph nodes extracted from mice at 12 h postinjection of PMCG, PMCG@NM, or PMCG@AM NGs. (B) Schematic illustration of the *in vivo* vaccination and tumor challenge process. Representative flow cytometry plots indicating the proportions of (C) $CD11c^+CD80^+$ DCs in lymph nodes and (D) $CD3^+CD8^+$ T cells in spleens after the mice were vaccinated for 3 times in different groups (n = 3). (E) The levels of TNF-α, IFN-γ and IFN-β in serum after the mice were vaccinated by different NGs (n = 3). (F) Individual tumor volume change of mice vaccinated by different NGs in tumor challenge assay (n = 6). Percentages of splenic (G) T_{EM} ($CD8^+CD44^+CD62L^-$ T cells) and (H) T_{CM} ($CD8^+CD44^+CD62L^+$ T cells) on day 21. In parts G and H, * is for $p < 0.05$, ** is for $p < 0.01$, and *** is for $p < 0.001$, respectively.

related proteins including phosphorylated STING, tank-binding kinase 1 (TBK1), and interferon regulatory factor 3 (IRF3) were analyzed by WB. As is known, the activated STING could bind and stimulate the TBK-1 to phosphorylate the IRF3, thus producing type I IFN. The expression levels of these three essential proteins increased after cells were treated with PMCG NGs, and reached the highest levels in PMCG@AM NGs group (Fig. S13, $p < 0.05$), confirming the STING pathway activation in the two types of immune cells. Overall, the PMCG@AM NGs can be phagocytosed by DCs or macrophages to deliver antigens and immune adjuvants, then effectively activate the STING pathway to mature DCs and repolarize macrophages.

3.4. *In vivo* vaccination and tumor challenge assay

After demonstrating the immune activation potential of PMCG@AM NGs *in vitro*, their activity in tumor prophylaxis was next investigated *in vivo*. First, we checked whether the PMCG@AM NGs were accumulated in lymph nodes, since the lymph node is one of the most important immune organs. Different NG formulations, including PMCG, PMCG@NM, and PMCG@AM NGs were subcutaneously injected at the left groin of healthy mice and the inguinal lymph nodes were collected and *ex vivo* imaged after 6 h or 12 h. As shown in Fig. S14, fluorescence signals were detected in all groups at 6 h postinjection, and the PMCG@AM group exhibited significantly higher fluorescence intensity at the lymph node than the other groups ($p < 0.01$). At 12 h post-injection, the fluorescence signals in the groups of PMCG and PMCG@NM decreased, while the PMCG@AM group still maintained a high fluorescence intensity (Fig. 4A), highlighting the advantages of the AM coating to promote the lymph node delivery and residence of NGs. Considering that the lymph node homing of NGs relies on the migration of matured DCs, we hypothesize that the decoration of AM could promote the phagocytosis of NGs by DCs and also boost the NG-mediated DC maturation.

To assess the PMCG@AM NG-induced immune responses, an *in vivo* vaccination assay was conducted and the treatment timeline is shown in Fig. 4B. Healthy mice were randomly divided into five groups and subcutaneously vaccinated with different NG formulations at the inguinal region for three times at a one-week interval. The populations of co-stimulatory markers (CD80 and CD86) on DCs extracted from lymph nodes nearby the injection site were first analyzed at 7 days post last vaccination. Compared to the percentages of $CD11c^+CD80^+$ DCs (2.3 %) and $CD11c^+CD86^+$ DCs (3.3 %) in the PMC NG group, the addition of cGAMP led to a higher level of DC maturation in the PMCG NG group as the percentages of $CD11c^+CD80^+$ DCs and $CD11c^+CD86^+$ DCs increased to 5.5 % and 7.1 %, respectively (Fig. 4C and Fig. S15). The expression levels of CD80 and CD86 on $CD11c^+$ DCs were further improved after the treatment with PMCG@NM NGs due to the co-delivery of TAAs carried by NM. As expected, mice vaccinated by PMCG@AM NGs displayed the highest proportions of $CD11c^+CD80^+$ DCs (9.4 %) and $CD11c^+CD86^+$ DCs (11.0 %) in lymph nodes among all groups, which may be derived from the AM coating with regulated immunogenicity for improved DC recognition, thus facilitating the best maturation of DCs.

It is well-known that matured DCs interact with naïve T cells to present TAAs and activate T cells, thus favoring the induction of a specific antitumor immune response [49]. Therefore, we next investigated the activation of splenic T cells on day 0 (7-day post the final vaccination). As shown in Figs. S16–S17 and Fig. 4D, PMCG@AM NGs enabled the most obvious proliferation of $CD3^+CD4^+$ T cells (52.7 %) and $CD3^+CD8^+$ T cells (27.8 %), reflecting that the codelivery of AM, MnO_2 NPs, and cGAMP by PMCG@AM NGs elicits the differentiation of effective T cells and cytotoxic T lymphocytes (CTLs) in spleens, both of which play essential roles in antitumor immunity. Meanwhile, the treatment of such a nanovaccine led to the highest expression levels of TNF-α, IFN-γ, and IFN-β in serum among all groups, indicating the successful activation of STING-mediated immune responses (Fig. 4E). Overall, the *in vivo* immune activation ability of PMCG@AM NGs was superior to PMCG@NM NGs since the AM with regulated immunoactivity could help PMCG@AM NGs be better recognized and swallowed by immune cells, thereby triggering enhanced antitumor immunity utilizing the presented AM and accumulated Mn/cGAMP.

Next, the effect of the PMCG@AM NG-induced immune response on tumor growth was investigated *in vivo*. After three times of vaccination by different NG formulations, mice were challenged with B16-F10 cells in their right hind leg at day 0. The individual tumor volume changes and average tumor growth curves showed that the vaccination with PMCG@AM NGs resulted in more efficient tumor inhibition compared to the other groups, consistent with the immune stimulating tendency (Fig. 4F and Fig. S18). To further confirm whether the vaccination of NGs can induce long-term antitumor immunity, splenocytes of mice were harvested again on day 21 and analyzed by flow cytometry to evaluate the percentages of memory T cells. As displayed in Fig. 4G–H and Fig. S19, the levels of both effector memory T cells (T_{EM}, $CD8^+CD44^+CD62L^-$ T cells) and central memory T cells (T_{CM}, $CD8^+CD44^+CD62L^+$ T cells) increased after vaccination by different NG formulations, and the highest elevation of memory T cells was found in the group of PMCG@AM NGs ($p < 0.001$). Generally, the immunization of PMCG@AM NGs generates a prophylactic effect to protect mice from tumor challenge and also successfully increases the expression of memory T cells in spleens, which means that activated T cells can quickly proliferate from memory T cells for tumor suppression.

3.5. *PMCG@AM NGs for in vitro CDT/SDT*

After discussing the capacity of PMCG@AM NGs as a nanovaccine, the direct tumor killing ability of PMCG@AM NGs was next evaluated to demonstrate the roles played by the loaded of MnO_2 NPs and Ce6 components. First, a CCK-8 assay was performed to investigate the cytotoxicity of PMCG@AM NGs against B16-F10 cells with or without US irradiation. As shown in Fig. S20, both the P NGs and free cGAMP seem to have considerable cytocompatibility as the cells treated with both materials showed reasonable viabilities even at a relatively high concentration. In contrast, PM NGs loaded with MnO_2 NPs showed significant cytotoxicity against B16-F10 cells compared to the PBS group ($p < 0.001$), probably because the decomposition of MnO_2 NPs consumes GSH and the generated Mn^{2+} produces ·OH (Fig. 5A). After further loading with the sonosensitizer Ce6, the cytotoxicity of PMC NGs slightly decreased before US irradiation, and the combined treatment of PMC NGs under US irradiation displayed a significantly enhanced toxicity to B16-F10 cells compared to the experiment without US ($p < 0.01$), suggesting that the application of US can activate Ce6 to exert the SDT effect on cells. Due to the promoted cellular uptake after cell membrane coating (Fig. 3A), the PMCG@NM and PMCG@AM NGs showed the most effective cancer cell killing efficiency compared to other NG formulations at the same Ce6 concentration (2 μg/mL) after US irradiation, resulting in around 45 % of cell viability.

To confirm the occurrence of CDT/SDT of NGs under US irradiation, the major indicators of the combination therapy, including intracellular GSH depletion, ROS generation, and $^1O_2$ production were analyzed. First, significant intracellular GSH depletion was observed in the PM NGs group, which is not only due to the consumption of GSH by MnO_2 NPs to form Mn^{2+}, but also because the formed Mn^{2+} is able to catalyze a Fenton-like reaction to generate ·OH, thus further decreasing the GSH levels (Fig. 5B). Furthermore, the groups of PMC NGs and PMCG NGs under US irradiation promoted much more GSH depletion, which should be ascribed to the Ce6-mediated $^1O_2$ production that can further consume GSH. With the assistance of AM or NM coating that enable enhanced cellular uptake, the groups of PMCG@NM and PMCG@AM NGs further displayed more significant GSH depletion ability than other groups ($p < 0.001$).

Subsequently, B16-F10 cells treated with different particles and US irradiation were stained by 2′, 7′-dichlorofluorescein diacetate (DCFH-

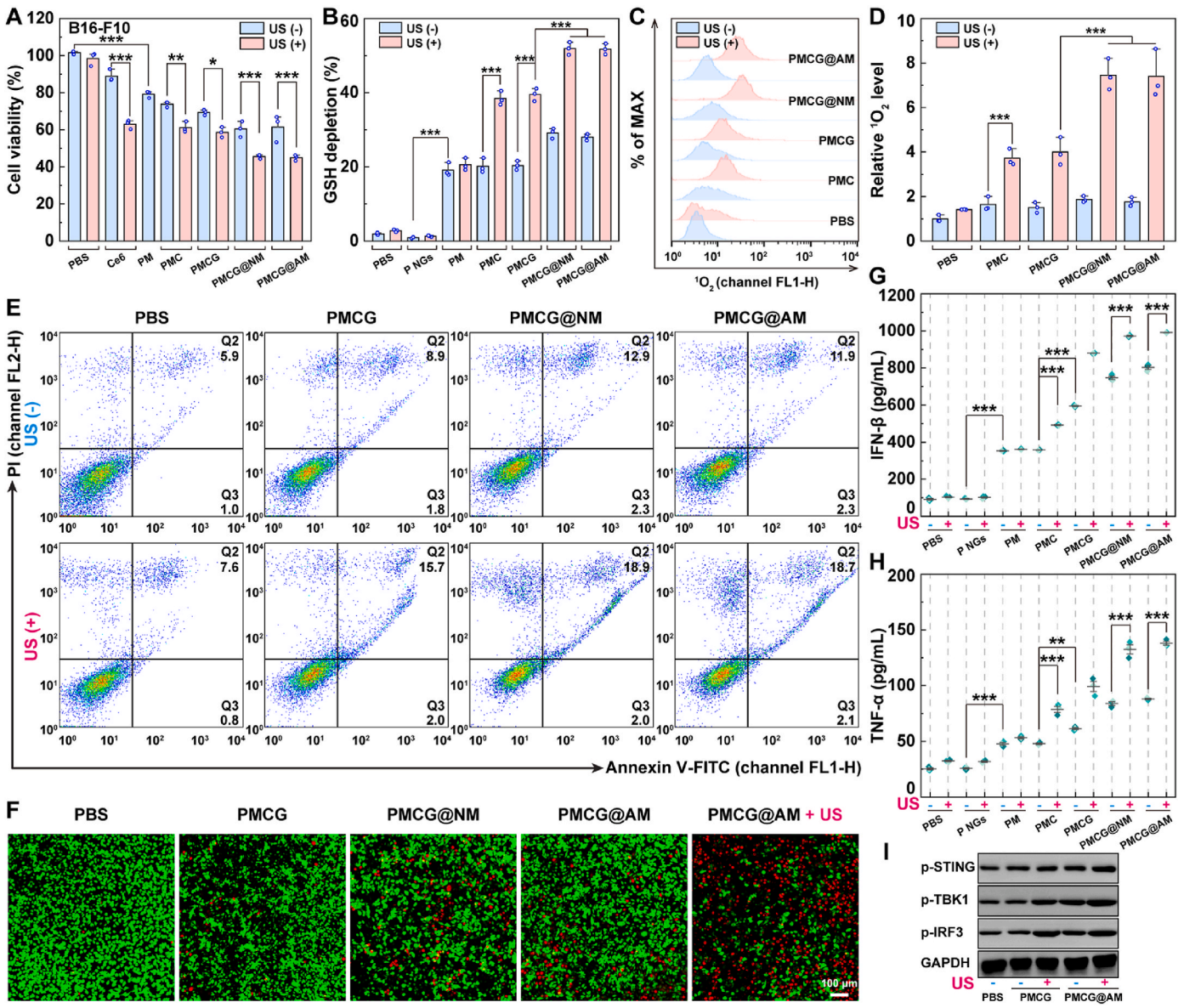

Fig. 5. (A) Viability of B16-F10 cells treated with Ce6 or different NGs at a Ce6 concentration of 2 μg/mL for 24 h with or without US irradiation (n = 6). (B) Intracellular GSH depletion in B16-F10 cells after different treatments for 6 h (n = 3). (C) Flow cytometry analysis and (D) quantification of intracellular $^1O_2$ level in B16-F10 cells after different treatments for 6 h (n = 3). (E) Flow cytometry analysis of B16-F10 cell apoptosis after different treatments for 12 h (n = 3). (F) CLSM of B16-F10 cells after different treatments and stained with LIVE/DEAD viability/cytotoxicity kit (green represents live cells, and red represents dead cells). Secretion of (G) IFN-β and (H) TNF-α in the culture medium of B16-F10 cells after different treatments (n = 3). (I) WB analysis of the expression of representative STING pathway-related proteins in B16-F10 cells after different treatments for 24 h. For (A–I), the parameters of US were set as: 1.0 MHz, 1.0 W/cm^2, and 2 min. In parts A-B, D, and G-H, * is for $p < 0.05$, ** is for $p < 0.01$, and *** is for $p < 0.001$, respectively.

DA) and observed by confocal laser scanning microscopy (CLSM) to verify the intracellular ROS levels (Fig. S21). As expected, cells treated with PM NGs displayed increased green fluorescence signals associated with enhanced ROS levels, and the employment of US enabled significantly improved intracellular ROS levels in all Ce6-containing groups, demonstrating the generation of ·OH catalyzed by Mn^{2+} and the production of $^1O_2$ induced by Ce6 + US. The PMCG@NM and PMCG@AM NGs led to the most significant ROS generation among all groups due to the enhanced cellular uptake.

To further validate the SDT effect, the production of $^1O_2$ after cells were treated with NGs under US was also evaluated using an O22 probe, which could be oxidized by $^1O_2$ to exhibit green fluorescence (Fig. 5C and D). Herein, we only tested the Ce6-containing NGs before and after US irradiation. Quantitative data from flow cytometry showed that all the NGs had no appreciable impact on the intracellular $^1O_2$ levels without US irradiation as the fluorescence intensity did not obviously change. Conversely, US irradiation significantly improved the fluorescence intensity in NG-treated B16-F10 cells, and the PMCG@NM and PMCG@AM NGs groups exhibited the highest fluorescence intensity among all groups ($p < 0.001$), demonstrating the enhanced generation of intracellular $^1O_2$.

We next evaluated the cell apoptosis rate of B16-F10 cells *via* flow cytometry. Due to the Mn-catalyzed CDT, the treatments with PMCG, PMCG@NM and PMCG@AM NGs without US irradiation induced 10.7 %, 15.2 %, and 14.2 % apoptotic cells, respectively (Fig. 5E and Fig. S22). With US irradiation, all the investigated NGs increased the apoptosis rate of the cells in all groups except for the PBS group ($p < 0.001$), indicating the prominent SDT effect on cell apoptosis. The PMCG@NM and PMCG@AM NGs exhibited a higher apoptosis rate than PMCG NGs due to the cancer cell membrane-facilitated enhanced

cellular uptake. In addition, live/dead cell staining assay was also performed to better visualize the combined therapeutic effect of CDT and SDT. As shown in Fig. 5F, similar to the tendency of the cell apoptosis assay, the treatment of PMCG@AM NGs plus US irradiation induced the most significant cell death (green fluorescence represents living cells, while red fluorescence represents dead cells).

3.6. PMCG@AM NGs for in vitro activation of STING in B16-F10 cells

Besides the proven ability of PMCG@AM NGs to activate the cGAS-STING pathway in immune cells to mature DCs and repolarize macrophages to the M1 type, we next measured the release of IFN-β and TNF-α from B16-F10 cells after different treatments to check whether the NGs could activate the cGAS-STING pathway in cancer cells. Before US irradiation, higher secretion levels of IFN-β and TNF-α were found in the PM and PMC NGs groups compared to the P NGs group, and the

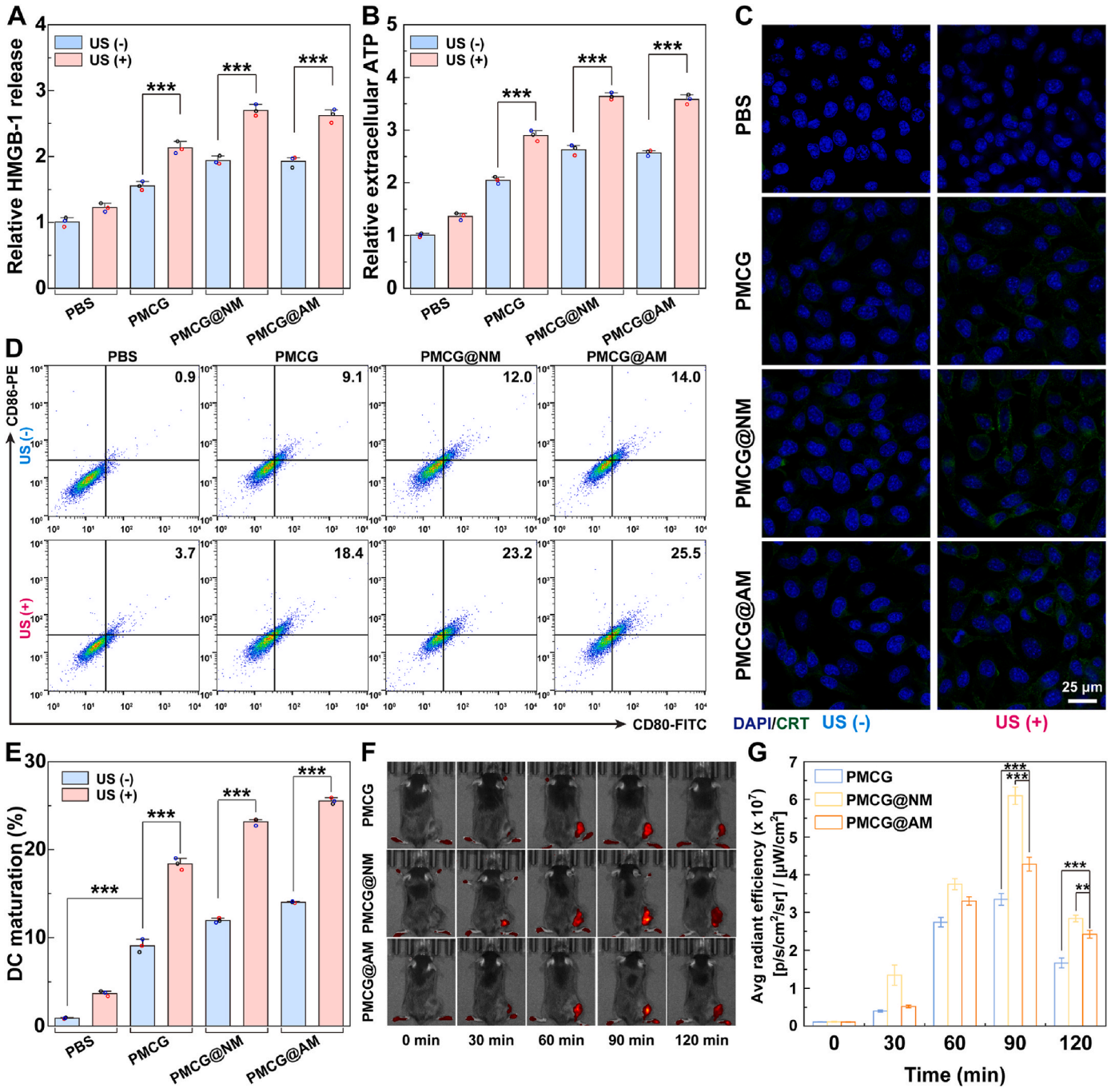

Fig. 6. (A) The release of HMGB-1 and (B) extracellular ATP secretion from B16-F10 cells after different treatments for 24 h (n = 3). (C) Immunofluorescence detection of CRT exposure on B16-F10 cells after different treatments for 24 h. (D) Flow cytometry analysis and (E) quantification of DC maturation after co-culturing with B16-F10 cells undergoing ICD (n = 3). (F) *In vivo* fluorescence images of B16-F10 tumor-bearing mice after intravenous injection of PMCG, PMCG@NM, or PMCG@AM NGs at different time points postinjection. (G) Quantitative fluorescence intensity of the tumor region at different time points post intravenous injection of PMCG, PMCG@NM, or PMCG@AM NGs (n = 3). For (A–E), the parameters of US were set as: 1.0 MHz, 1.0 W/cm^2, and 2 min. In parts A-B, E, and G, * is for $p < 0.05$, ** is for $p < 0.01$, and *** is for $p < 0.001$, respectively.

treatment of PMCG NGs further improved the cytokine expression levels, indicating that Mn^{2+} in coordination with cGAMP enables the enhanced activation of cGAS-STING pathway in B16-F10 cells to promote the release of related cytokines (Fig. 5G and H). Notably, US irradiation significantly boosted the production of cytokines in all Ce6-containing groups, likely due to the SDT-generated abundant ROS that can induce DNA damage and the damaged DNA can be recognized by cGAS to further activate the STING pathway, in good accordance with the literature [31].

To further confirm the effect of PMCG@AM NGs plus US irradiation on STING pathway activation in B16-F10 cells, the expression of related proteins, including phosphorylated STING, TBK1, and IRF3 was next detected *via* a WB assay. Compared with the PMCG NGs group, the higher expression levels of p-STING, p-TBK1, and p-IRF3 were achieved in PMCG NGs + US group, suggesting the essential role of US irradiation to sensitize the STING pathway (Fig. 5I and Fig. S23). Moreover, the PMCG@AM NGs + US group induced the most obvious upregulation of the three STING-related proteins due to the AM-promoted cellular uptake, reconfirming the capacity of PMCG@AM NGs to activate the STING pathway of cancer cells with the help of US for inducing immunity.

3.7. PMCG@AM NGs for in vitro ICD induction

Except for triggering immune responses *via* the STING pathway, CDT and SDT are also promising to induce the ICD of cancer cells to release damage-associated molecular patterns, thus stimulating the immune system. Therefore, the changes of three major ICD indicators, including the release of high mobility group protein 1 (HMGB-1) and adenosine 5′-triphosphate (ATP), as well as the CRT exposure on B16-F10 cells were evaluated after different treatments. As shown in Fig. 6A–C, the treatment of PMCG NGs alone increased the release of HMGB-1 and ATP, and promoted the translocation of CRT to the cell surface, demonstrating the positive role of Mn^{2+}-mediated CDT in inducing ICD. Strikingly, the treatment of PMCG NGs plus US irradiation led to significantly enhanced HMGB-1 release and ATP secretion ($p < 0.001$), as well as increased green fluorescence signals associated with CRT on the cell surface, since the participation of SDT can amplify the ICD effect. NM- or AM-coated PMCG NGs with US irradiation displayed the strongest ICD effect among all groups due to the improved cellular uptake.

Subsequently, the *in vitro* DC maturation induced by cancer cells undergoing ICD was analyzed using a transwell system. The maturation rate of DCs was quantitatively analyzed by flow cytometry to check the percentages of $CD80^{+}CD86^{+}$ DCs after treatments. Without US irradiation, the treatment of PMCG NGs led to moderate DC maturation (9.1 %), and the PMCG@NM and PMCG@AM NGs slightly increased the DC maturation rate to 12.0 % and 14.0 %, respectively (Fig. 6D and E), and significantly increased the DC maturation rate to 23.2 % and 25.5 % with US irradiation due to the US-triggered SDT. It is worth noting that not only the ICD of treated cancer cells can promote DC maturation, but also the activation of the STING pathway in cancer cells can mature DCs utilizing the released cytokines.

All these *in vitro* assays led us to conclude that the PMCG@AM NGs are able to not only directly stimulate immune cells, but also enable efficient CDT and SDT on cancer cells with the assistance of US, thus further triggering immune responses to complete the full-cycle immunomodulation for better tumor treatment (see below).

3.8. In vivo fluorescence imaging and biodistribution

Before using PMCG@AM NGs for *in vivo* tumor therapy, we first evaluated their *in vivo* tumor targeting efficiency *via* fluorescence imaging in a subcutaneous mouse tumor model. PMCG@NM and PMCG NGs were also tested for comparison. The fluorescence images of B16-F10 tumor-bearing mice at different time points post intravenous injection of different NG formulations are displayed in Fig. 6F. The fluorescence intensity at the tumor site in the PMCG NGs group first increased to reach a maximum at 90 min postinjection, and then decreased. The considerable tumor accumulation of PMCG NGs can be attributed to the enhanced permeability and retention effect-based passive tumor delivery. Upon the injection of PMCG@NM NGs, the fluorescence signals of the tumor region were significantly higher than when PMCG NGs were administrated at each time point, confirming that the decoration of NM can facilitate active tumor targeting. Most noteworthy, the subcutaneous tumor in the PMCG@AM NGs group exhibited lower fluorescence intensity than in the PMCG@NM NGs group at the same time point, likely due to fact that the AM-camouflaged NGs are more easily recognized and phagocytosed by immune cells, thus hindering their tumor accumulation to some degree. The quantitative analysis of tumor fluorescence intensity shows the same tendency as the fluorescence images, reconfirming the enhanced fluorescence signals at the tumor site after injection with PMCG@NM NGs (Fig. 6G). Importantly, the PMCG@AM NGs exhibited higher tumor fluorescence intensity than PMCG NGs, especially after 60 min, which indicates that the AM decoration is still able to render the NGs with tumor targeting to some extent.

To further validate the biodistribution of PMCG, PMCG@NM, or PMCG@AM NGs, the *ex vivo* fluorescence imaging of major organs and tumors was next performed at 120 min postinjection (Fig. S24). Compared to the PMCG NGs group, treatment with PMCG@NM NGs led to decreased fluorescence intensity in liver and lung, and increased tumor fluorescence intensity, reconfirming the improved tumor targeting ability after coating with NM. Moreover, the PMCG@AM NGs group exhibited enhanced Ce6 fluorescence intensity in lung and decreased fluorescence intensity in tumor in comparison to the group of PMCG@NM NGs. Remarkably, the strongest fluorescence signals of the spleen were found in the PMCG@AM NGs group, proving that the decoration with AM caused improved NGs capture by immune cells, leading to accumulation in immune organs.

Lastly, the long-term biodistribution of NM/AM-coated NGs in tumor-bearing mice was quantitatively analyzed by ICP-OES at 48 h postinjection (Fig. S25). Clearly, the PMCG@AM NGs displayed higher Mn uptake in spleen and lung than the PMCG@NM NGs, and lower Mn uptake in tumor than the PMCG@NM NGs, in consistence with the results of fluorescence imaging. To sum up, the PMCG@NM NGs could better be accumulated in tumors and the PMCG@AM NGs could better be captured by immune organs.

3.9. In vivo tumor treatment and immune activation

To investigate the *in vivo* tumor suppression efficiency of PMCG@AM NGs plus US irradiation, a bilateral B16-F10 mouse tumor model was established according to the timeline illustrated in Fig. 7A. When the primary tumor reached about 100 mm^3, the targeting efficiency of PMCG@AM NGs to bilateral tumors was first assessed through detecting the Mn contents in both primary and distant tumors after intravenous administration. As shown in Fig. S26, the Mn contents in both primary and distant tumors showed no significant difference at three different time points, suggesting that the NGs have equal targeting specificity to the bilateral B16-F10 tumors.

Then, the tumor-bearing mice were subjected to different treatments *via* intravenous administration of PBS, PMCG, PMCG@NM, or PMCG@AM NGs. For PMCG@AM NGs + US group, only the primary tumors were exposed to US irradiation at 90 min postinjection. It was found that the mice in all groups showed a slight increase in body weight during 14 days, suggesting that the designed NGs did not cause severe side effects (Fig. S27A). As shown in Fig. 7B–C and Fig. S27B, the treatment of PMCG NGs alone resulted in a moderate inhibition effect on both the primary and distant tumors, possibly due to the Mn^{2+}-mediated CDT. The PMCG@NM and PMCG@AM NGs, due to the cell membrane decoration displayed enhanced tumor accumulation, thus showing better suppression efficacy on bilateral tumors than PMCG NGs.

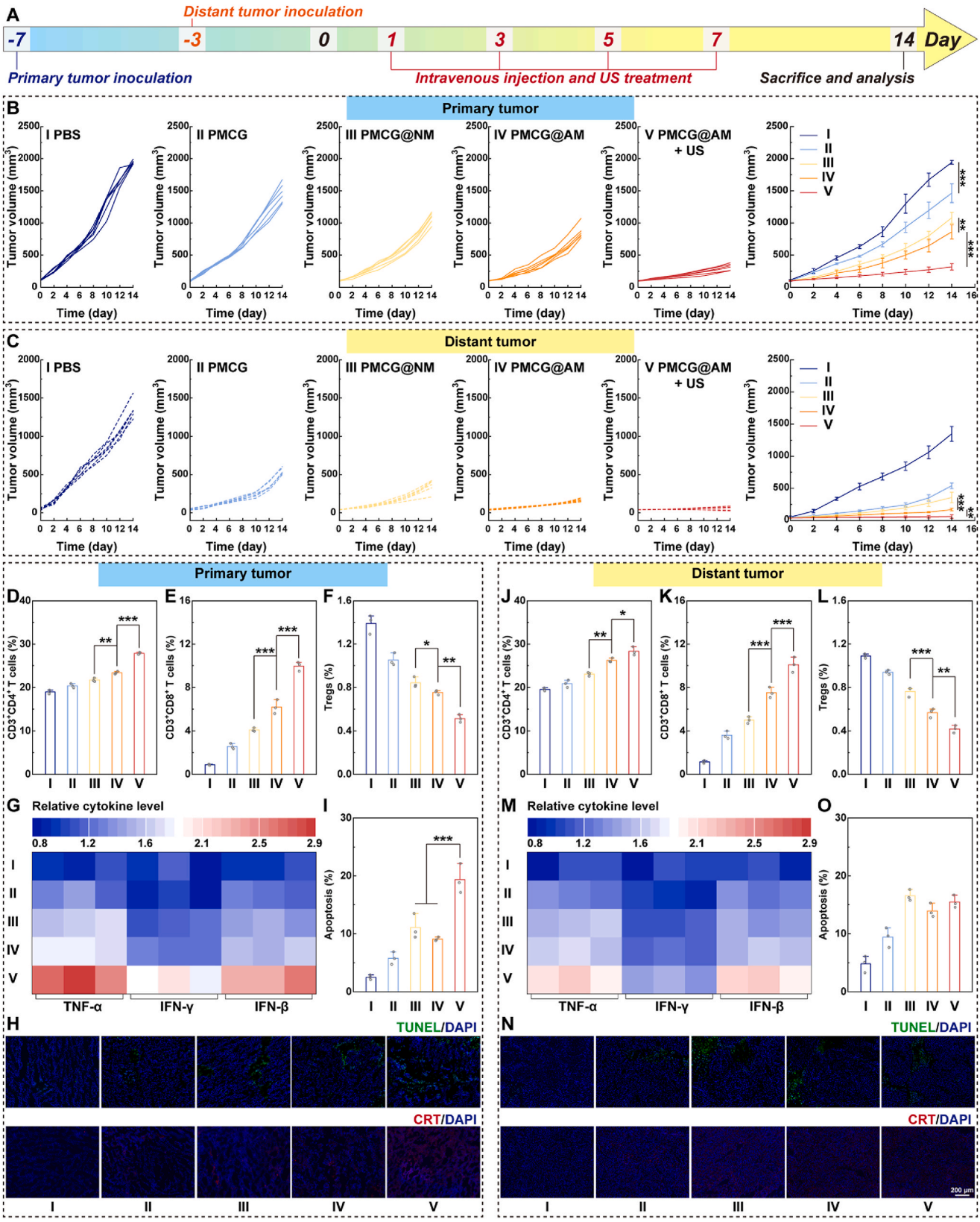

Fig. 7. (A) Schematic illustration of the *in vivo* antitumor assay. (B) Primary and (C) distant tumor volume change of B16-F10 tumor-bearing mice after different treatments (n = 6). Percentages of $CD3^+CD4^+$ T cells, $CD3^+CD8^+$ T cells, and Tregs in (D–F) primary tumors or (J–L) distant tumors after different treatments (n = 3). The levels of TNF-α, IFN-γ and IFN-β in (G) primary tumors or (M) distant tumors after different treatments (n = 3). TUNEL staining of apoptotic tumor cells and immunofluorescence staining of CRT in (H) primary tumors or (N) distant tumors after the mice were treated for 14 days in different groups. The apoptosis rate of tumor cells in (I) primary tumors or (O) distant tumors after different treatments (n = 3). For (A–O), the parameters of US were set as: 1.0 MHz, 1.0 W/cm^2, and 5 min. In parts B-F, J-L, I and O, * is for $p < 0.05$, ** is for $p < 0.01$, and *** is for $p < 0.001$, respectively.

Moreover, the treatment of PMCG@AM NGs + US not only clearly inhibited the primary tumor growth ($p < 0.001$) through the combined CDT and US-triggered SDT, but also efficiently delayed the growth of the distant tumors ($p < 0.01$) on the 14th day. The occurrences of CDT and SDT in the primary tumors were confirmed through immunofluorescence staining of ROS. As shown in Fig. S28, without US irradiation, the treatments with different NG formulations were able to increase the red fluorescence intensity, which means that Mn^{2+} has triggered CDT in primary tumors to generate ROS. The addition of US irradiation led to a significant increase of intratumoral ROS levels in the PMCG@AM NGs + US group, indicating the generation of $^1O_2$ inside tumors *via* Ce6-mediated SDT. Besides, it is important to note that the growth rate of distant tumors was much lower than that of the primary tumors. Furthermore, even though the PMCG@AM NGs showed less tumor accumulation, they exhibited a better tumor inhibition performance than PMCG@NM NGs. We assume that in addition to CDT and SDT, the created immune responses induced by the different treatments play a crucial role in tumor growth inhibition.

To verify the above hypothesis, the immune cells were extracted at the 14th day post treatments for flow cytometry analysis. First, the DCs in primary tumor-draining lymph nodes were harvested to analyze the maturation of DCs *via* testing of the CD80 and CD86 expression levels. As shown in Fig. S29, the PMCG@AM NGs + US group promoted the percentages of both $CD11c^+CD86^+$ DCs (9.4 %) and $CD11c^+CD80^+$ DCs (10.6 %) to a level much higher than the other groups ($p < 0.001$), which means that the combination of PMCG@AM NGs and US irradiation is able to significantly mature DCs *in vivo* through the induction of ICD or direct activation of DCs as demonstrated in the *in vitro* assays. Then, the tumor-infiltrating T cells in bilateral tumors were extracted for flow cytometry analysis of the $CD3^+CD4^+$/$CD3^+CD8^+$ T cells, as well as the regulatory T cells (Tregs, $CD4^+CD25^+Foxp3^+$ T cells). The PMCG@AM NGs plus US irradiation led to the highest populations of intratumoral $CD3^+CD4^+$ T cells and $CD3^+CD8^+$ T cells in both primary (Fig. 7D–E and Figs. S30–S31) and distant tumors (Fig. 7J–K and Figs. S32–S33), along with the lowest populations of intratumoral Tregs in primary (Fig. 7F and Fig. S34) and distant tumors (Fig. 7L and Fig. S35). Despite the tumor-infiltrating T cells, the phenotypes of tumor-associated macrophages (TAMs) were also evaluated *via* immunofluorescence staining of inducible nitric oxide synthase (iNOS, a marker for M1-type macrophages) and arginase-1 (Arg-1, a marker for M2-type macrophages) in distant tumor sections (Fig. S36). The most decreased Arg-1 level and increased iNOS level were observed in the PMCG@AM NGs + US group, suggesting that the PMCG@AM NGs + US can trigger the most efficient immune responses in distant tumors to repolarize TAMs and also recruit M1-type TAMs, consistent with the *in vitro* data (Fig. S12). Lastly, ELISA showed that the expression levels of representative antitumor-associated cytokines, including TNF-α, IFN-γ, and IFN-β increased in both primary tumors (Fig. 7G) and distant tumors (Fig. 7M) after treatment with different NG formulations. The levels of these three cytokines in the primary tumors significantly increased in the PMCG@AM NGs + US group, since the US irradiation on primary tumors can induce more immune responses *via* local SDT/CDT than *via* CDT only. Taken together, the PMCG@AM NGs under US irradiation allowed for efficient induction of antitumor immune responses, thus limiting the growth of distant tumors. Notably, the PMCG@AM NGs always induced better antitumor immunity than PMCG@NM NGs due to the regulated immunostimulatory capability of AM, which proves our hypothesis that the PMCG@AM NGs with regulated immunogenicity can induce a more potent immune response to realize more efficient tumor suppression than the PMCG@NM NGs.

Subsequently, the mechanism of PMCG@AM NGs + US to efficiently suppress bilateral tumor growth was further confirmed by TdT-mediated dUTP Nick-End Labeling (TUNEL) staining of tumor sections, as well as the immunofluorescence staining of CRT in tumor sections. Herein, TUNEL staining was used to check the percentages of tumor cell apoptosis, while the CRT staining was used to indicate the ICD degree. As displayed in Fig. 7H–I, 7N-O, and Fig. S37, in both primary tumors and distant tumors, the tumor apoptosis rate and CRT-positive level followed the order of PBS < PMCG NGs < PMCG@AM NGs < PMCG@NM NGs, consistent with the tendency of tumor accumulation as demonstrated in fluorescence imaging (Fig. 6F and G), indicating that the NGs can be accumulated in bilateral tumors to induce apoptosis and ICD through the triggered CDT effect. The group of PMCG@AM NGs + US showed the most significantly enhanced apoptosis and CRT exposure in the primary tumors among all groups. However, this is not the same case for the distant tumors, since the distant tumors did not receive US irradiation, and the group of PMCG@NM showed the most significant tumor apoptosis and CRT exposure due to the improved distant tumor accumulation of the NGs that can only induce CDT effect.

3.10. Biosafety evaluation

Lastly, the *in vivo* biocompatibility of PMCG@AM NGs + US was analyzed. First, the major organs of mice after treatment with PBS or PMCG@AM NGs + US were harvested and H&E stained (Fig. S38). Clearly, no appreciable pathological abnormalities were observed in all major organs, suggesting that the administration of PMCG@AM NGs plus local US irradiation has no organ toxicity to mice. Then, PMCG@AM NGs were used to treat healthy mice for hematology and serum biochemistry analysis at 7 days postinjection. As shown in Fig. S39, PMCG@AM NGs displayed no significant influence on the tested blood routine indexes (white blood cell, WBC; red blood cell, RBC; and hemoglobin, HGB), liver function parameters (aspartate aminotransferase, AST; and alanine aminotransferase, ALT), as well as kidney parameter (blood urea nitrogen, BUN), which further indicates the desired biosafety profile of the PMCG@AM NGs.

4. Conclusion

In summary, we report an innovative design of a therapeutic nanovaccine based on AM camouflaged PVCL NGs loaded with MnO_2, the sonosensitizer Ce6 and the immune adjuvant cGAMP (PMCG@AM NGs). The presence of these therapeutic agents allows the NGs to directly stimulate immune cells through STING activation and antigen presentation, thereby activating T cells for preventing tumor growth. The PMCG@AM NGs can furthermore selectively trigger CDT at tumor sites and activate SDT under local US irradiation, thus significantly inhibiting the growth of bilateral tumors through the combined SDT/CDT-mediated ICD and immune modulation. Our results suggest that the synthesized PMCG@AM NGs can make full use of the antigenicity of AM, MnO_2 and cGAMP to wake up the immune system against specific tumors, and the precise CDT/SDT can also induce immune responses to reinforce the antitumor immunity through the cycle of ICD-mediated DC maturation and T cell activation, thus realizing a full-cycle immunomodulation for prevention of tumor occurrence and comprehensive tumor combination CDT/SDT/immunotherapy.

Ethics approval and consent to participate

All animal experiments were performed in accordance with the guidelines of the Committee on Experimental Animal Care and Use of Donghua University (approval # DHUEC-NSFC-2023-02) and also in accordance with the regulations of the National Ministry of Health of China.

The authors declare that they have no known competing financial interests or personal relationships that could have appeared to influence the work reported in this paper.

CRediT authorship contribution statement

Yunqi Guo: Writing – original draft, Visualization, Methodology, Investigation, Formal analysis, Data curation, Conceptualization.

Zhiqiang Wang: Visualization, Validation, Software, Methodology, Formal analysis, Data curation. **Gaoming Li:** Validation, Methodology, Investigation, Data curation. **Mengsi Zhan:** Software, Formal analysis, Data curation. **Tingting Xiao:** Investigation, Formal analysis, Data curation. **Jianhong Wang:** Methodology, Investigation. **Jan C.M. van Hest:** Writing – review & editing, Supervision, Resources, Funding acquisition. **Xiangyang Shi:** Writing – review & editing, Supervision, Resources, Project administration, Funding acquisition, Conceptualization. **Mingwu Shen:** Writing – review & editing, Supervision, Resources, Project administration, Funding acquisition, Conceptualization.

Declaration of competing interest

The authors declare that they have no known competing financial interests or personal relationships that could have appeared to influence the work reported in this paper.

Acknowledgements

This study was financially supported by the National Natural Science Foundation of China (U23A2096 and 52350710203), the Science and Technology Commission of Shanghai Municipality (23520712500, 21490711500, and 20DZ2254900), and the Netherlands Ministry of Education, Culture and Science (Gravitation Program Interactive Polymer Materials 024.005.020, Gravitation Program Materials Driven Regeneration 024.003.013 and the Spinoza premium SPI 72–259). Scheme 1, Fig. 2A–. 3D, and ToC are created with BioRender.com.

Appendix A. Supplementary data

Supplementary data to this article can be found online at https://doi.org/10.1016/j.bioactmat.2024.09.024.

References

[1] L. Zhou, W.Z. Yi, Z.H. Zhang, X.T. Shan, Z.T. Zhao, X.S. Sun, J. Wang, H. Wang, H. L. Jiang, M.Y. Zheng, D.G. Wang, Y.P. Li, STING agonist-boosted mRNA immunization *via* intelligent design of nanovaccines for enhancing cancer immunotherapy, Natl. Sci. Rev. 10 (10) (2023) nwad214.

[2] W.L. Liu, M.Z. Zou, T. Liu, J.Y. Zeng, X. Li, W.Y. Yu, C.X. Li, J.J. Ye, W. Song, J. Feng, X.Z. Zhang, Cytomembrane nanovaccines show therapeutic effects by mimicking tumor cells and antigen presenting cells, Nat. Commun. 10 (1) (2019) 3199.

[3] L. Chen, H. Qin, R.F. Zhao, X. Zhao, L.R. Lin, Y. Chen, Y.X. Lin, Y. Li, Y.T. Qin, Y. Y. Li, S.L. Liu, K.M. Cheng, H.Q. Chen, J. Shi, G.J. Anderson, Y. Wu, Y.L. Zhao, G. J. Nie, Bacterial cytoplasmic membranes synergistically enhance the antitumor activity of autologous cancer vaccines, Sci. Transl. Med. 13 (601) (2021) eabc2816.

[4] Y.Z. Su, W.G. Xu, Q. Wei, Y. Ma, J.X. Ding, X.S. Chen, Chiral polypeptide nanoparticles as nanoadjuvants of nanovaccines for efficient cancer prevention and therapy, Sci. Bull. 68 (3) (2023) 284–294.

[5] I. Melero, G. Gaudernack, W. Gerritsen, C. Huber, G. Parmiani, S. Scholl, N. Thatcher, J. Wagstaff, C. Zielinski, I. Faulkner, H. Mellstedt, Therapeutic vaccines for cancer: an overview of clinical trials, Nat. Rev. Clin. Oncol. 11 (9) (2014) 509–524.

[6] R. Yang, J. Xu, L.G. Xu, X.Q. Sun, Q. Chen, Y.H. Zhao, R. Peng, Z. Liu, Cancer cell membrane-coated adjuvant nanoparticles with mannose modification for effective anticancer vaccination, ACS Nano 12 (6) (2018) 5121–5129.

[7] X.M. Hu, T.T. Wu, X.Y. Qin, Y. Qi, Q. Qiao, C.L. Yang, Z.P. Zhang, Tumor lysate-loaded lipid hybrid nanovaccine collaborated with an immune checkpoint antagonist for combination immunotherapy, Adv. Healthcare Mater. 8 (1) (2019) 1800837.

[8] H.M. Xia, M.M. Qin, Z.H. Wang, Y.Q. Wang, B.L. Chen, F.J. Wan, M.M. Tang, X. Q. Pan, Y. Yang, J.X. Liu, R.Y. Zhao, Q. Zhang, Y.G. Wang, A pH-/enzyme-responsive nanoparticle selectively targets endosomal toll-like receptors to potentiate robust cancer vaccination, Nano Lett. 22 (7) (2022) 2978–2987.

[9] F.M. Chen, T.L. Li, H.J. Zhang, M. Saeed, X.Y. Liu, L.J. Huang, X.Y. Wang, J. Gao, B. Hou, Y. Lai, C.Y. Ding, Z.A. Xu, Z.Q. Xie, M. Luo, H.J. Yu, Acid-ionizable iron nanoadjuvant augments STING activation for personalized vaccination immunotherapy of cancer, Adv. Mater. 35 (10) (2023) 2209910.

[10] Z.L. Gao, W. Xu, S.J. Zheng, Q.J. Duan, R. Liu, J.Z. Du, Orchestrated cytosolic delivery of antigen and adjuvant by manganese ion-coordinated nanovaccine for enhanced cancer immunotherapy, Nano Lett. 23 (5) (2023) 1904–1913.

[11] C.C. Feng, P. Tan, G.J. Nie, M.T. Zhu, Biomimetic and bioinspired nano-platforms for cancer vaccine development, Exploration 3 (3) (2023) 20210263.

[12] W. Lei, C. Yang, Y. Wu, G.Q. Ru, X.L. He, X.M. Tong, S.B. Wang, Nanocarriers surface engineered with cell membranes for cancer targeted chemotherapy, J. Nanobiotechnol. 20 (1) (2022) 45.

[13] X. Xiong, J.Y. Zhao, J.M. Pan, C.P. Liu, X. Guo, S.B. Zhou, Personalized nanovaccine coated with calcinetin-expressed cancer cell membrane antigen for cancer immunotherapy, Nano Lett. 21 (19) (2021) 8418–8425.

[14] R.H. Fang, Y. Jiang, J.C. Fang, L.F. Zhang, Cell membrane-derived nanomaterials for biomedical applications, Biomaterials 128 (2017) 69–83.

[15] Y.Q. Guo, Y. Fan, Z.Q. Wang, G.M. Li, M.S. Zhan, J.L. Gong, J.P. Majoral, X.Y. Shi, M.W. Shen, Chemotherapy mediated by biomimetic polymeric nanoparticles potentiates enhanced tumor immunotherapy *via* amplification of endoplasmic reticulum stress and mitochondrial dysfunction, Adv. Mater. 34 (47) (2022) 2206861.

[16] Y.Q. Guo, Z.Q. Wang, X.Y. Shi, M.W. Shen, Engineered cancer cell membranes: an emerging agent for efficient cancer theranostics, Exploration 2 (1) (2022) 20210171.

[17] S.Y. Shen, Y. Gao, Z.J. Ouyang, B.Y. Jia, M.W. Shen, X.Y. Shi, Photothermal-triggered dendrimer nanovaccines boost systemic antitumor immunity, J. Controlled Release 355 (2023) 171–183.

[18] Y.X. Guo, S.Z. Wang, X.P. Zhang, H.R. Jia, Y.X. Zhu, X.D. Zhang, G. Gao, Y. W. Jiang, C.C. Li, X.K. Chen, S.Y. Wu, Y. Liu, F.G. Wu, *In situ* generation of micrometer-sized tumor cell-derived vesicles as autologous cancer caccines for boosting systemic immune responses, Nat. Commun. 13 (1) (2022) 6534.

[19] D.V. Krysko, A.D. Garg, A. Kaczmarek, O. Krysko, P. Agostinis, P. Vandenabeele, Immunogenic cell death and DAMPs in cancer therapy, Nat. Rev. Cancer 12 (12) (2012) 860–875.

[20] A.D. Garg, D. Nowis, J. Golab, P. Vandenabeele, D.V. Krysko, P. Agostinis, Immunogenic cell death, DAMPs and anticancer therapeutics: an emerging amalgamation, Biochim. Biophys. Acta, Rev. Cancer 1805 (1) (2010) 53–71.

[21] H.D. Zhu, K. Ma, R. Ruan, C.B. Yang, A.Q. Yan, J. Li, Q. Yu, H.M. Sun, M.X. Liu, H. M. Zheng, J. Gao, X.F. Guan, Z. Dai, Y. Sun, Tumor-targeted self-assembled micelles reducing PD-L1 expression combined with ICIs to enhance chemo-immunotherapy of TNBC, Chin. Chem. Lett. 35 (2) (2024) 108536.

[22] S.H. van der Burg, R. Arens, F. Ossendorp, T. van Hall, C.J.M. Melief, Vaccines for established cancer: overcoming the challenges posed by immune evasion, Nat. Rev. Cancer 16 (4) (2016) 219–233.

[23] X.S. Li, J.F. Lovell, J.Y. Yoon, X.Y. Chen, Clinical development and potential of photothermal and photodynamic therapies for cancer, Nat. Rev. Clin. Oncol. 17 (11) (2020) 657–674.

[24] P.R. Zhao, H.Y. Li, W.B. Bu, A forward vision for chemodynamic therapy: issues and opportunities, Angew. Chem., Int. Ed. 62 (7) (2023) e202210415.

[25] V. Choi, M.A. Rajora, G. Zheng, Activating drugs with sound: mechanisms behind sonodynamic therapy and the role of nanomedicine, Bioconjugate Chem. 31 (4) (2020) 967–989.

[26] S.B. Son, J.H. Kim, X.W. Wang, C.L. Zhang, S.A. Yoon, J.W. Shin, A. Sharma, M. H. Lee, L. Cheng, J.S. Wu, J.S. Kim, Multifunctional sonosensitizers in sonodynamic cancer therapy, Chem. Soc. Rev. 49 (11) (2020) 3244–3261.

[27] Y.J. Li, W. Chen, Y. Kang, X.Y. Zhen, Z.M. Zhou, C. Liu, S.Y. Chen, X.G. Huang, H. J. Liu, S.Y. Koo, N. Kong, X.Y. Ji, T. Xie, W. Tao, Nanosensitizer-mediated augmentation of sonodynamic therapy efficacy and antitumor immunity, Nat. Commun. 14 (1) (2023) 6973.

[28] S. Liang, J.J. Yao, D. Liu, L. Rao, X.Y. Chen, Z.H. Wang, Harnessing nanomaterials for cancer sonodynamic immunotherapy, Adv. Mater. 35 (33) (2023) 2211130.

[29] X.W. Zhang, X.C. Bai, Z.J.J. Chen, Structures and mechanisms in the cGAS-STING innate immunity pathway, Immunity 53 (1) (2020) 43–53.

[30] Y.X. Zhao, X.C. Ye, Z.F. Xiong, A. Ihsan, I. Ares, M. Martínez, B. Lopez-Torres, M. R. Martínez-Larrañaga, A. Anadón, X.W. Wang, M.A. Martínez, Cancer metabolism: the role of ROS in DNA damage and induction of apoptosis in cancer cells, Metabolites 13 (7) (2023) 796.

[31] X.J. Zhao, R.J. Zheng, B.B. Zhang, Y. Zhao, W.L. Xue, Y.F. Fang, Y.W. Huang, M. Z. Yin, Sulfonated perylene as three-in-one STING agonist for cancer chemo-immunotherapy, Angew. Chem., Int. Ed. (2024), https://doi.org/10.1002/anie.202318799.

[32] C. Chen, P.L. Xu, Cellular functions of cGAS-STING signaling, Trends Cell Biol. 33 (8) (2023) 630–648.

[33] J. Yang, Y.P. He, M. Zhang, C.L. Liang, T.T. Li, T.J. Ji, M.L. Zu, X. Ma, Z.Z. Zhang, C. Liang, Q.X. Zhang, Y.B. Chen, L. Hou, Programmed initiation and enhancement of cGAS/STING pathway for tumour immunotherapy via tailor-designed $ZnFe_2O_4$-based nanosystem, Exploration 3 (6) (2023) 20230061.

[34] L.F. Deng, H. Liang, M. Xu, X.M. Yang, B. Burnette, A. Arina, X.D. Li, H. Mauceri, M. Beckett, T. Darga, X.N. Huang, T.F. Gajewski, Z.J.J. Chen, Y.X. Fu, R. R. Weichselbaum, STING-dependent cytosolic DNA sensing promotes radiation-induced type I interferon-dependent antitumor immunity in immunogenic tumors, Immunity 41 (5) (2014) 843–852.

[35] S.R. Woo, M.B. Fuertes, L. Corrales, S. Spranger, M.J. Furdyna, M.Y.K. Leung, R. Duggan, Y. Wang, G.N. Barber, K.A. Fitzgerald, M.L. Alegre, T.F. Gajewski, STING-dependent cytosolic DNA sensing mediates innate immune recognition of immunogenic tumors, Immunity 41 (5) (2014) 830–842.

[36] Z.T. Zhao, Z.X. Ma, B. Wang, Y.K. Guan, X.D. Su, Z.F. Jiang, Mn^{2+} directly activates cGAS and structural analysis suggests Mn^{2+} induces a noncanonical catalytic synthesis of 2′3′-cGAMP, Cell Rep. 32 (7) (2020) 108053.

[37] M.Z. Lv, M.X. Chen, R. Zhang, W. Zhang, C.G. Wang, Y. Zhang, X.M. Wei, Y. K. Guan, J.J. Liu, K.C. Feng, M. Jing, X.R. Wang, Y.C. Liu, Q. Mei, W.D. Han, Z. F. Jiang, Manganese is critical for antitumor immune responses *via* cGAS-STING and improves the efficacy of clinical immunotherapy, Cell Res. 30 (11) (2020) 966–979.

[38] C.G. Wang, Y.K. Guan, M.Z. Lv, R. Zhang, Z.Y. Guo, X.M. Wei, X.X. Du, J. Yang, T. Li, Y. Wan, X.D. Su, X.J. Huang, Z.F. Jiang, Manganese increases the sensitivity of the cGAS-STING pathway for double-stranded DNA and is required for the host defense against DNA viruses, Immunity 48 (4) (2018) 675–687.
[39] X.Q. Sun, Y. Zhang, J.Q. Li, K.S. Park, K. Han, X.W. Zhou, Y. Xu, J. Nam, J. Xu, X. Y. Shi, L. Wei, Y.L. Lei, J.J. Moon, Amplifying STING activation by cyclic dinucleotide–manganese particles for local and systemic cancer metalloimmunotherapy, Nat. Nanotechnol. 16 (11) (2021) 1260–1270.
[40] Y. Gao, Z.J. Ouyang, S.Y. Shen, H.W. Yu, B.Y. Jia, H. Wang, M.W. Shen, X.Y. Shi, Manganese dioxide-entrapping dendrimers co-deliver protein and nucleotide for magnetic resonance imaging-guided chemodynamic/starvation/immune therapy of tumors, ACS Nano 17 (23) (2023) 23889–23902.
[41] C.C. Zhang, W.Z. Tu, X.M. Chen, B. Xu, X. Li, C.L. Hu, M.W. Shen, S.L. Song, C. J. Jiang, S.Y. Yao, A. Pich, Y. Liu, X.Y. Shi, Intelligent design of polymer nanogels for full-process sensitized radiotherapy and dual-mode computed tomography/magnetic resonance imaging of tumors, Theranostics 12 (7) (2022) 3420–3437.
[42] F. Xu, J.Z. Zhu, L.Z. Lin, C.C. Zhang, W.J. Sun, Y. Fan, F.F. Yin, J.C.M. van Hest, H. Wang, L.F. Du, X.Y. Shi, Multifunctional PVCL nanogels with redox-responsiveness enable enhanced MR imaging and ultrasound-promoted tumor chemotherapy, Theranostics 10 (10) (2020) 4349–4358.
[43] B.Y. Jia, Y. Gao, Z.J. Ouyang, S.Y. Shen, M.W. Shen, X.Y. Shi, Diselenide-crosslinked nanogels laden with gold nanoparticles and methotrexate for immunomodulation-enhanced chemotherapy and computed tomography imaging of tumors, J. Mater. Chem. B 11 (21) (2023) 4808–4818.
[44] T.T. Xiao, M.J. He, F. Xu, Y. Fan, B.Y. Jia, M.W. Shen, H. Wang, X.Y. Shi, Macrophage membrane-camouflaged responsive polymer nanogels enable magnetic resonance imaging-guided chemotherapy/chemodynamic therapy of orthotopic glioma, ACS Nano 15 (12) (2021) 20377–20390.
[45] L.S. Lin, J.B. Song, L. Song, K.M. Ke, Y.J. Liu, Z.J. Zhou, Z.Y. Shen, J. Li, Z. Yang, W. Tang, G. Niu, H.H. Yang, X.Y. Chen, Simultaneous fenton-like ion delivery and glutathione depletion by MnO_2-based nanoagent to enhance chemodynamic therapy, Angew. Chem., Int. Ed. 57 (18) (2018) 4902–4906.
[46] C. Gu, X.L. Liu, L. Luo, J.Q. Chen, X. Zhou, G.H. Chen, X.J. Huang, L. Yu, Q. Chen, Y. Yang, Y. Yang, Metal-DNA nanocomplexes enhance chemo-dynamic therapy by inhibiting autophagy-mediated resistance, Angew. Chem., Int. Ed. 62 (50) (2023) e202307020.
[47] Z.M. Tang, P.R. Zhao, H. Wang, Y.Y. Liu, W.B. Bu, Biomedicine meets fenton chemistry, Chem. Rev. 121 (4) (2021) 1981–2019.
[48] Y. Chen, D.L. Ye, M.Y. Wu, H.R. Chen, L.L. Zhang, J.L. Shi, L.Z. Wang, Break-up of two-dimensional MnO_2 nanosheets promotes ultrasensitive pH-triggered theranostics of cancer, Adv. Mater. 26 (41) (2014) 7019–7026.
[49] K. Palucka, J. Banchereau, Cancer immunotherapy *via* dendritic cells, Nat. Rev. Cancer 12 (4) (2012) 265–277.